ESPOO 2008 VTT PUBLICATIONS 684

Jussi Hiltunen

Microstructure and superlattice effects on the optical properties of ferroelectric thin films

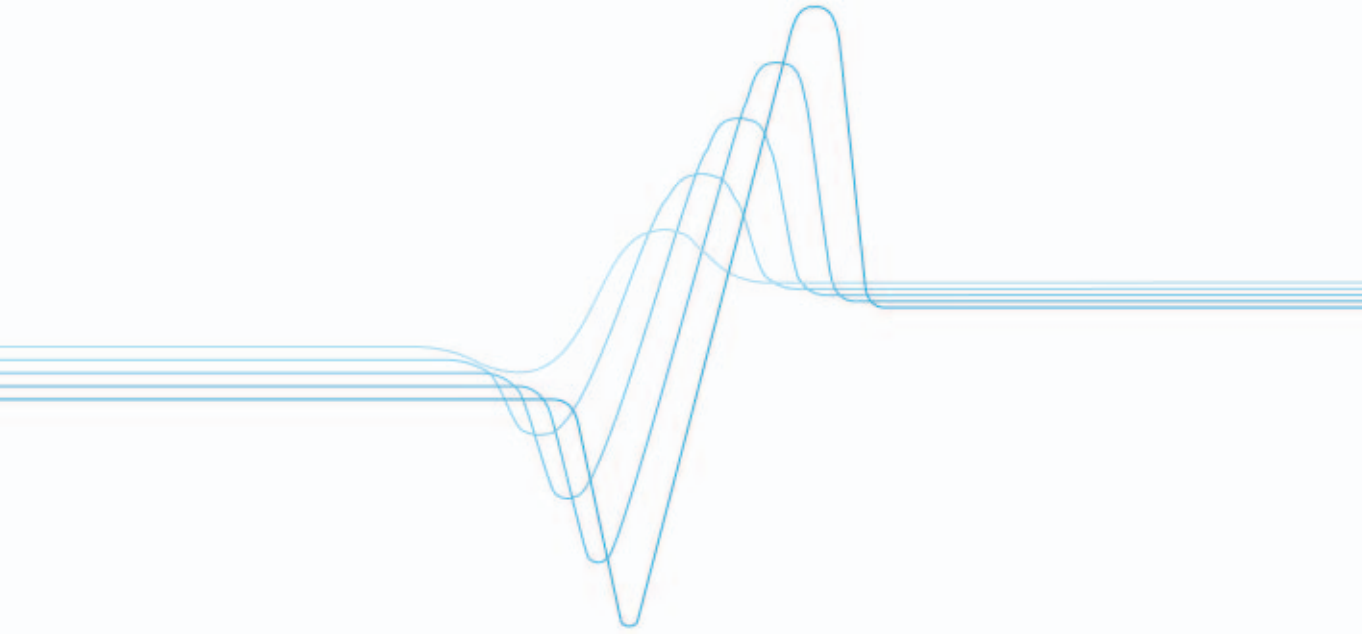

Infotech Oulu

VTT PUBLICATIONS 684

Microstructure and superlattice effects on the optical properties of ferroelectric thin films

Jussi Hiltunen

Academic Dissertation to be presented with the assent of the Faculty of Technology, University of Oulu, for public discussion in Raahensali (Auditorium L10), Linnanmaa, on June 27th, 2008, at 12 noon.

ISBN 978-951-38-7102-4 (soft back ed.)
ISSN 1235-0621 (soft back ed.)

ISBN 978-951-38-7103-1 (URL: http://www.vtt.fi/publications/index.jsp)
ISSN 1455-0849 (URL: http://www.vtt.fi/publications/index.jsp)

JULKAISIJA – UTGIVARE – PUBLISHER

VTT, Vuorimiehentie 3, PL 1000, 02044 VTT
puh. vaihde 020 722 111, faksi 020 722 4374

VTT, Bergsmansvägen 3, PB 1000, 02044 VTT
tel. växel 020 722 111, fax 020 722 4374

VTT Technical Research Centre of Finland, Vuorimiehentie 3, P.O.Box 1000, FI-02044 VTT, Finland
phone internat. +358 20 722 111, fax +358 20 722 4374

VTT, Kaitoväylä 1, PL 1100, 90571 OULU
puh. vaihde 020 722 111, faksi 020 722 2320

VTT, Kaitoväylä 1, PB 1100, 90571 ULEÅBORG
tel. växel 020 722 111, fax 020 722 2320

VTT Technical Research Centre of Finland, Kaitoväylä 1, P.O. Box 1100, FI-90571 OULU, Finland
phone internat. +358 20 722 111, fax +358 20 722 2320

Technical editing Anni Repo

Hiltunen, Jussi. Microstructure and superlattice effects on the optical properties of ferroelectric thin films. Espoo 2008. VTT Publications 684. 82 p. + app. 42 p.

Keywords ferroelectrics, thin film, electro-optics, superlattice, PZT, $BaTiO_3$, $SrTiO_3$

Abstract

This thesis deals with the microstructure effects on the optical properties of *(i)* polycrystalline Nd-modified lead-zirkonium-titanate (PNZT) and *(ii)* highly oriented $BaTiO_3$ (BTO) thin films together with the stacking structure influence on the optical properties of *(iii)* $BaTiO_3$–$SrTiO_3$ (STO) superlattice thin films. All the films were grown on MgO(001) substrates by pulsed laser deposition. Different structures were obtained by tuning the thin film processing conditions.

PNZT thin films were deposited at room temperature and different crystallite size distributions were produced by varying the post-annealing temperature. The refractive index and electro-optic responses were found to increase with increasing mean crystallite size.

Oxygen pressure during the film deposition at 700 °C was found to be a very critical parameter to modify the crystallographic and consequent other physical properties of BTO thin films as suggested by the dielectric and optical measurements. Low oxygen pressure films were epitaxial, with elongated lattice parameters along the surface normal, while increased working oxygen pressure produced non-epitaxial films with lattice elongation along the in-plane orientation. An effective electro-optic coefficient of ~21 pm/V was measured for the BTO films.

Periodic BTO-STO superlattices were deposited with varying stacking periodicity between 27 and 1670 Å. Birefringence decreased with increasing stacking periodicity, due to relaxation of the lattice strain induced by the layer interfaces. The electro-optic response was found to reach a maximum at a specific stacking periodicity and it decreases with both increasing and decreasing individual layer thickness. The operation of a Mach-Zehnder waveguide intensity modulator based on the BTO-STO superlattice with effective electro-optic coefficient of 73 pm/V was also demonstrated.

Preface

The work covered by this thesis has been carried out at VTT Technical Research Centre of Finland in collaboration with the University of Oulu during the years 2002–2008. The author has been participating in the graduate school of Infotech Oulu. A significant part of the research was performed at Massachusetts Institute of Technology, USA, during 2005–2006.

I greatly thank Professors Vilho Lantto (University of Oulu), Harri Kopola (VTT) and Pentti Karioja (VTT) for introducing this interesting research field, their encouragement and guidance during the work, and also, providing the supporting projects. I warmly express my gratitude to Prof. Harry L. Tuller (MIT) for the possibility to work at Crystal Physics and Electroceramics Laboratory, and for his continual advice.

Professors Pekka Kuivalainen and Markus Pessa are acknowledged for reviewing the thesis manuscript.

Especially, I would like to thank Dr. Jyrki Lappalainen for his advice in the several phases of the work. I express also special thanks to Dr. Terho Kololuoma and Dr. Dilan Seneviratne for their valuable help.

I acknowledge the financial support from Tekes – the Finnish Funding Agency for Technology and Innovation, Infotech Oulu, the Academy of Finland, Finnish Foundation for Technology Promotion, Tauno Tönningin säätiö, Emil Aaltosen säätiö and Seppo Säynäjäkankaan tiedesäätiö.

I am grateful to the other co-authors and researchers who have contributed to this work. In Oulu: Mr. Jarkko Tuominen, Mr. Markus Tuomikoski, Mr. Mikko Karppinen, Dr. Janne Aikio, Mr. Jarkko Puustinen and Mr. Teemu Alajoki, Mrs. Sanna Uusitalo and Mr. Risto Karjalainen. And in Boston: Mr. Rong Sun, Dr. Michael Stolfi, Dr. Il-Doo Kim, Dr. Woo-Sik Kim, Mr. Scott Litzelman, Dr. Avner Rothschild, Dr. Joshua Hertz and Mr. Vikram Sivakumar. I am also most indebted to the other staff at VTT, University of Oulu and MIT for providing various kinds of assistance needed to carry out this work and creating an inspiring and pleasant working environment.

I would like to thank my family and parents-in-law for the support. Finally, my loving thanks go to my wife Maiju, son Ilari and daughter Elise for their patience and encouragement.

List of original publications

The present thesis consists of the following five papers, which will be referred to in the text by their Roman numerals (Papers I–V).

I Lappalainen, J., Hiltunen, J. and Lantto, V. 2005. Characterization of optical properties of nanocrystalline doped PZT thin films. Journal of the European Ceramic Society, Vol 25, pp. 2273–2276.

II Hiltunen, J., Seneviratne, D., Tuller, H. L., Lappalainen, J. and Lantto, V. 2008. Crystallographic and dielectric properties of highly oriented $BaTiO_3$ films: Influence of oxygen pressure utilized during pulsed laser deposition. Journal of Electroceramics, published online 8 March 2008, 10 p. DOI 10.1007/s10832-008-9443-0.

III Hiltunen, J., Seneviratne, D., Sun, R., Stolfi, M., Tuller, H. L., Lappalainen, J. and Lantto, V. 2008. Optical properties of $BaTiO_3$ thin films: Influence of oxygen pressure utilized during pulsed laser deposition. Journal of Electroceramics, published online 7 March 2008, 5 p. DOI 10.1007/s10832-008-9463-9.

IV Hiltunen, J., Lappalainen, J., Puustinen, J., Lantto, V. and Tuller, H. L. 2008. Size-dependent optical properties of $BaTiO_3$–$SrTiO_3$ superlattices. Optics Express, Vol. 16, No. 11, pp. 8219–8228.

V Hiltunen, J., Seneviratne, D., Sun, R., Stolfi, M., Tuller, H. L., Lappalainen, J. and Lantto, V. 2006. $BaTiO_3$ – $SrTiO_3$ multilayer thin film electro-optic waveguide modulator. Applied Physics Letters, Vol. 89, Article 242904, 3 p.

The contributions of the papers included in the thesis are:

Paper I describes the influence of the crystallite size distribution on the optical and electro-optical properties of Nd-modified $PbZr_xTi_{1-x}O_3$ thin films. Different crystal size distributions were obtained by varying the annealing temperature.

The refractive index and electro-optic response of the thin films were found to increase with increasing mean grain size.

Paper II reports on the manipulation of the crystal orientation of BTO thin films by adjusting the deposition parameters, and how the changes in microstructure are transferred to dielectric properties. Thin films deposited at low oxygen pressure were epitaxial with elongated lattice parameter along the surface normal, while increased working oxygen pressure produced non-epitaxial films with lattice elongation along the in-plane orientation. The influence of the crystal reorientation was observed in dielectric measurements. The initially symmetric tuning curves of permittivity became almost linear in samples with elongated lattice along the in-plane direction as a result of the poling treatment.

Paper III reports how the changes in the BTO microstructure are transferred to the optical properties. The consequence of crystal reorientation, suggested by the x-ray diffraction and electrical measurements, was clearly observed in direction-depended refractive index measurements with the change of sign of the optical birefringence. Also, optical waveguide devices were manufactured to evaluate the suitability of thin films with different microstructure in planar optical applications and to characterize the electro-optical properties of the thin films.

Paper IV shows that optical properties of BTO-STO superlattices are sensitive to the stacking periodicity. Birefringence decreases with increasing stacking periodicity due to relaxation of the interface induced stress. The electro-optic response of BTO-STO superlattices was found to reach a maximum value at a specific stacking periodicity.

Paper V is the first publication on the operation of the Mach-Zehnder optical waveguide modulator based on the ferroelectric-paraelectric superlattices. It demonstrates the potential suitability of BTO-STO superlattices in planar optical devices.

The contribution of the author of this thesis is as following:

– The author of the thesis was the main author of the Papers II–V and contributed to the both research and manuscript preparation of Paper I.

– All the studied thin films were grown by the author except in Paper I, where the films were grown by Dr. Jyrki Lappalainen.

– Optical and electro-optical properties of the thin films were characterized by the author in Papers I and IV and waveguide measurements with the kind help of Mr. Rong Sun in Papers III and V.

– The author contributed to the waveguide process development with significant work of Dr. Dilan Seneviratne in Papers III and V.

– X-ray diffraction studies in Papers II and V were made by the author and in Paper IV together with Mr. Jarkko Puustinen.

– The permittivity studies described in Paper II were made by the author.

Other papers related to this work, but not included in the thesis:

– Lappalainen, J., Lantto, V., Frantti, J. and Hiltunen, J. 2006. X-ray diffraction and Raman investigations of thickness dependent stress effects on $Pb(Zr_xTi_{1-x})O_3$ thin films. Applied Physics Letters, Vol. 88, Article 252901.

– Lappalainen, J., Frantti, J., Hiltunen, J., Lantto, V. and Kakihana, M. 2006. Stress and Film Thickness Effects on the Optical Properties of Ferroelectric $Pb(Zr_xTi_{1-x})O_3$ Films. Ferroelectrics, Vol. 335, pp. 149–158.

– Kololuoma, T., Hiltunen, J., Tuomikoski, M., Lappalainen, J. and Rantala, J. 2004. Directly UV-photopatternable PLZT thin films prepared with the Sol-Gel technique. Proceedings of SPIE. Vol. 5355. Integrated Optics: Devices, Materials, and Technologies VIII. Pp. 33–39.

In additional papers the author carried out the transmittance and electro-optic measurements.

The work was carried out in collaboration between VTT and the University of Oulu during 2002–2008. Part of the work was done at the Massachusetts Institute of Technology (USA) during 2005–2006.

Contents

Appendices I–V of the publication are not included in this PDF version. Please order the printed version to get the complete publication (http://www.vtt.fi/publications/index.jsp)

List of symbols and abbreviations

a	atomic scattering factor
A	amplitude of the electric field (A_{TE}, A_{TM})
c	speed of light
c_0	speed of light in vacuum
d	unit cell length
E	electric-field
F	structure factor
g	electrode gap
I	intensity
J	Jones matrix
L	electrode length
n	refractive index
n_o	ordinary refractive index in birefringent crystal
n_e	extraordinary refractive index in birefringent crystal
$n_{x,y,z}$	refractive index along the principal x-, y- or z-axis
$n_{x',z'}$	refractive index along the rotated x'- or z'-axis
P_S	spontaneous polarization

q	length of scattering vector
r	linear electro-optic coefficient
r_{eff}	effective electro-optic coefficient
R	the second order electro-optic coefficient
T	rotation matrix
T_{c}	Curie temperature
V	voltage
V_{π}	voltage inducing a phase shift of π in an electro-optic device
W	phase shift matrix
α	polarization angle
$\delta\Delta n$	shift in birefringence
ε	permittivity
ε_0	vacuum permittivity
ε_{r}	relative permittivity
φ	optical phase retardation
Γ	overlap factor
λ	wavelength

AFM	atomic force microscope
BST	barium strontium titanate ($Ba_xSr_{1-x}TiO_3$)
BTO	barium titanate ($BaTiO_3$)
CPU	central processing unit
CSC	chemical solution coating
EO	electro-optic
FE	ferroelectric
FWHM	full width at half maximum
IDE	inter-digital-electrode
LNO	lithium niobate
MBE	molecular beam epitaxy
MOCVD	metalorganic chemical vapor deposition
OEIC	optoelectronics integrated circuit
OIC	optical integrated circuit
PE	paraelectric
PLD	pulsed laser deposition
PNZT	Nd-modified lead-zirkonate-titanate $(Pb_{1-3/2y}\,Nd_y)(Zr_xTi_{1-x})O_3$
PZT	lead-zirkonate-titanate $Pb(Zr_xTi_{1-x})O_3$
RMS	root mean square

SEM	scanning electron microscope
STO	strontium titanate ($SrTiO_3$)
TE	transverse electric field
TM	transverse magnetic field
XRD	x-ray diffraction

1. Introduction

1.1 Optoelectronics integrated circuits

A typical optoelectronics system consists of three main parts [1, 2]. 1) Compound semiconductor alloy devices are commonly utilized to generate light. This is followed by the 2) transmission of light, possibly including also amplification or signal manipulation, and finally 3) intensity sensing by semiconductor photodiodes. These systems are utilized, for example, in data communication and instrumentation applications. A wide range of different materials are required to perform the required functionalities and conventionally main approach has been to use discrete components.

In order to produce more functionality with a reduced number of required discrete components on separate platforms, an optical integrated circuit (OIC) or optoelectronics integrated circuit (OEIC) concept has been developed. In OEICs, optical circuits are designed to produce a certain function by integrating the required devices on a single substrate [1, 2, 3]. An example of integrated-optic transmitter/receiver device is shown in Figure 1. Light from a laser is guided, modulated, and coupled into a fiber, while received light is coupled into a waveguide and directed to a photodiode, where it is detected.

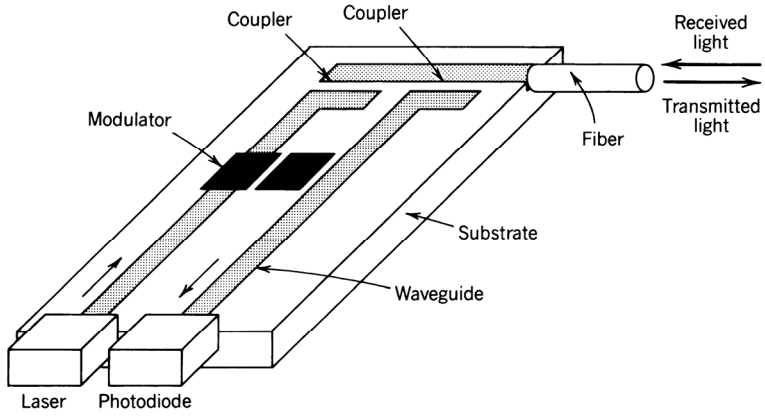

Figure 1. An example of an integrated-optic device used as an optical receiver/transmitter [4].

Ultimately, the operation of all active and passive devices (laser diodes, switches, modulators, waveguides and detectors) can be produced in a single material. This is called a monolithic OEIC. Since light generation is required, monolithic circuits can only be fabricated on substrates capable of producing light, typically being semiconductors with direct band gap.

Another approach is to use hybrid techniques, in which the OEIC devices are made of different materials and integrated together allowing more flexible use of material choices and processes [2, 5]. This can include various techniques, like thin film vacuum or liquid phase deposition of desired materials. In this case, the materials compatibility and the coefficients of thermal expansion must be considered if high temperature processes are used. Another option is to joint separately processed components on a single substrate, when the processing conditions can be relaxed. However, very tight alignment accuracy may be required with components assembly. A typical case is the alignment between a laser and optical fiber or waveguide when sub micrometer accuracy is preferable in single mode technology [2, 6].

1.2 Active waveguiding thin films

Waveguiding structures are required in OEICs to transmit optical signals between devices. Waveguides can be classified into two categories: passive structures exhibiting static light guiding characteristics, and functional devices for the active optical wave control [7]. The functionality may include the control of the optical signal routing or intensity modulation. The activity in guiding media can be generated for example by acousto-, magneto-, thermo- or electro-optic effects [8]. So called ferroelectric materials are of interest for active light guiding devices due to the advantages of many of their functional properties [9]. One example of optical ferroelectric materials is $LiNbO_3$ (LNO), an electro-optic (EO) crystal widely used as a substrate for active waveguide devices [10].

Thin film waveguide technology is considered as an attractive alternative for the discrete component approach in photonics applications, because it can offer an opportunity to use a wide variety of materials that are not processable in bulk form and also allowing to achieve a high level of component integration with reduced size [11]. Ferroelectric thin films have been grown by several

processing techniques, such as sputtering [12] , chemical solution coating (CSC) [12, 13], pulsed-laser-deposition (PLD) [12, 14, 15], metalorganic-chemical-vapor-deposition (MOCVD) [12] and molecular-beam-epitaxy (MBE) [16]. Typically, the physical properties of ferroelectric thin films are moderate as compared to those in bulk due to the substrate induced strain, stress relaxation induced crystal defects and film thickness effects [12]. However, devices demonstrating the feasibility of ferroelectric thin films in photonics applications have been fabricated, e.g. lead-zirkonium-titanate (PZT) acousto-optic Bragg reflectors [17] and barium-titanate (BTO) electro-optic waveguide modulator with potential up to 40 GHz range operation [18].

Important issues in active waveguides, besides the strong externally induced optical functionality, are the propagation properties and the intensity attenuation mechanisms setting high quality requirements for the thin films. The attenuation has several origins including absorption, scattering and the conversion between wave modes inside the guiding structure with varying propagation properties [19, 20]. Light with wavelength not inducing interband electronic transitions can be absorbed in defects either within a crystal or at grain boundaries [19]. Scattering loss is a result of random variation of refractive index contrast and may occur both inside the guiding film and at surfaces. This is considered the major loss for many dielectric devices [19]. Inside the film, inhomogeneities may result from undesired phases among the main crystal phase, the mixing of anisotropic grain orientation in single-phase film and also at grain boundaries [20]. Scattering due to surface inhomogeneity is also known to be very sensitive on surface roughness with RMS level of about 1 nm considered desirable [20].

1.3 Motivation of this thesis

The physical properties of macroscopic bulk PZT and BTO based ceramics have been extensively studied [21, 22]. In thin film form physical properties are often very different from the ones in bulk and commonly sensitive on processing conditions, such as, temperature, deposition rate, working pressure etc. As these materials have been shown to be promising candidates also in thin film optical applications, different microstructure effects on the optical properties in these compounds were studied. BTO-STO superlattices are known to have a very high tunability of permittivity, and therefore their suitability for the optical

applications were evaluated. Pulsed laser deposition technique was utilized in this work to deposit all the thin films having the advantage of the simplicity of the experimental setup and the possibility to grow films from complex multi-composition targets. The purpose of this experimental work on the optical properties of ferroelectric thin films was:

1. The development of fabrication technologies to manufacture electro-optic waveguiding devices based on the ferroelectric thin films. This includes the optimization of the thin film growth conditions to obtain optical quality ferroelectric thin films together with the development of waveguide manufacturing processes by lithographic techniques.

2. The properties of ferroelectric materials are sensitive to the crystal size distribution in the media. The understanding of the influence of crystallite distribution in ferroelectric (PZT) thin film on the optical properties is relevant if these type of structures are to be used in applications. In this work, the static refractive index and the electro-optic response change with varying grain size distribution was studied.

3. The microstructure of pulsed laser deposited BTO thin films depends on oxygen pressure during the deposition. In addition, BTO has been demonstrated to be a good material candidate for functional photonics devices. Therefore, the influence of oxygen partial pressure on the electrical and optical properties of BTO thin films was studied and the usability of differently processed films in waveguide devices was evaluated.

4. Ferroelectric-paraelectric superlattice thin films possess stacking periodicity dependent nonlinear permittivity. High tunability of the permittivity has been obtained by optimizing the stacking structure. As very little data was available on optical properties of superlattice thin films, the studies on these materials were included in this thesis. The studied structures were BTO (ferroelectric) – STO (paraelectric) superlattices.

2. Some properties of ferroelectrics

2.1 Polarization and dielectric properties

Dielectric materials possessing spontaneous polarization state that can be shifted from one state to another are called ferroelectrics [21]. A ferroelectric crystal possesses an actual ferroelectric phase only below a specific temperature. At high temperatures, the crystal is paraelectric phase. The crystal undergoes a structural phase transition from paraelectric (PE) non-polar phase to a polarized ferroelectric (FE) phase, when the temperature decreases through the Curie temperature (T_c). The exact transition temperature is dependent on crystallite size, rate of temperature variation, stress condition and purity of the material [22]. Typically PE-FE transition is followed by several FE-FE phase transitions with decreasing temperature [9, 21]. An example of this is $BaTiO_3$ (BTO) that commonly serves as a model ferroelectric [21–24]. BTO is a ferroelectric material, which is widely studied both theoretically and experientially. It possesses excellent functional properties that offer applications in microelectronics and photonics. It has a Curie temperature between 120 and 130 °C, where the paraelectric cubic crystal structure changes to tetragonal structure with electrical polarization along the tetragonal axes as shown in Figure 2 [21–25]. The structure is the perovskite structure that is very typical for a family of ferroelectric materials and all the materials studied in this work have this perovskite structure.

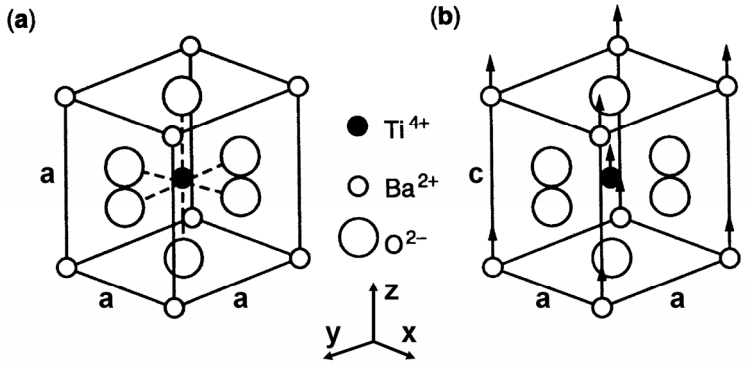

Figure 2. The crystal structure of $BaTiO_3$: (a) above the Curie temperature, the unit cell is cubic with lattice constant a; (b) below the Curie temperature, the cell is tetragonal with lattice constants a and c. Ba^{2+} and Ti^{4+} ions are now displaced relative to O^{2-} ions along the z-axis [24].

At about 5 °C BTO transforms to an orthorhombic phase and finally to a rhomboedral phase below –90 °C. Physical properties show large anomalies near the transition temperatures. This is illustrated in Figure 3(a), where the permittivity is plotted as a function of temperature in the vicinity of PE-FE phase transition temperature and in (b) and (c) the behavior of polarization as a function of electric field is described above and below the transition temperature, respectively.

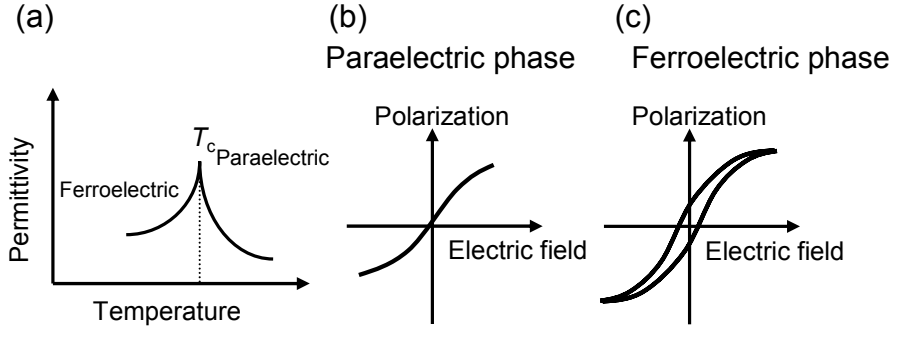

Figure 3. (a) Typical evolution of permittivity in the vicinity of paraelectric-ferroelectric transition Curie temperature T_C. (b) and (c) show polarization behavior as a function of electric field in ferroelectric material above and below the Curie temperature T_C , respectively [26].

Below the Curie temperature T_c alignment of dipoles occur in the direction of tetragonal axis in a certain volume of a crystal called a ferroelectric domain. An important characteristic of ferroelectrics is the hysteresis between the polarization and electric field as illustrated in Figure 3(c). When the external electric field is removed, the domains maintain partly their orientation and a stable remanent polarization remains.

Especially Sr-modified BTO compounds $Ba_xSr_{1-x}TiO_3$ (BST) have been widely studied due to their high nonlinearity of permittivity, which can be utilized in tunable microwave circuits. BST can be categorized as a solid solution of BTO and STO. While STO is a paraelectric material with no ferroelectric transition, the Curie temperature of the BST solution can be tuned. The room temperature phase is ferroelectric when x>0.5–0.7 [27, 28]. Also, increased thermal stability can be obtained by combining paraelectric and ferroelectric layers with opposite drift of permittivity as a function temperature [29]. Besides the electronics applications, BST has been also considered as an interesting material in thin-film electro-optic devices [30]. So-called relaxor ferroelectrics consisting of nano-domains without permanent macroscopic polarization are attractive in electronic and optical applications due to their very high and nonlinear polarization properties [9, 31, 32]. A large hysteresis of some ferroelectric compounds are utilized in non-volatile memory devices [9, 33].

2.2 Optical properties

Ferroelectric materials are interesting from many points of view in the field of optics. This interest is based on the multitude of phenomena that ferroelectric crystals exhibit, such as optical birefringence, electro-optic activity and nonlinear effects. In isotropic dielectric medium, the electric permittivity ε is defined as

$$\varepsilon = \varepsilon_r \varepsilon_0 , \tag{1}$$

where ε_0 is the permittivity of free space and ε_r the relative permittivity. The permittivity describes the material polarizability under external electric field and the net polarization in dielectric material consists of several frequency dependent

mechanisms illustrated in Figure 4, where a typical polarizability for a dielectric is plotted as a function of frequency.

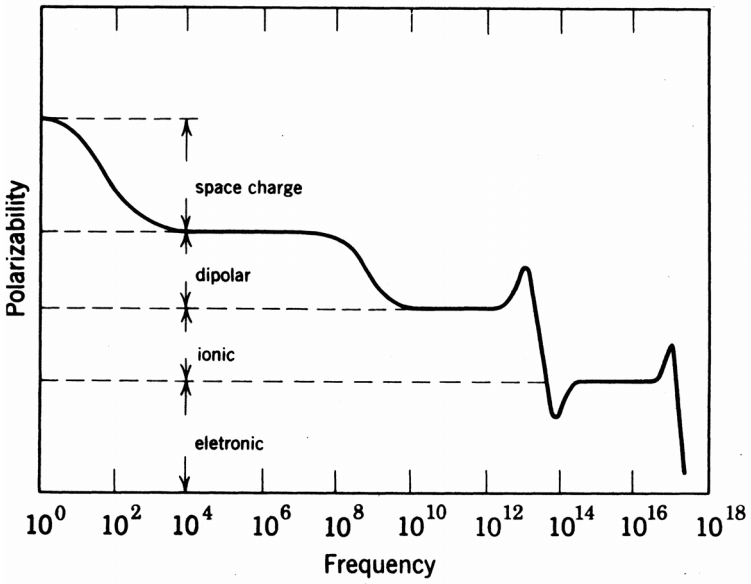

Figure 4. Polarizability as a function of frequency [34].

Since light is an alternating electromagnetic wave with electric and magnetic field vibration directions mutually perpendicular to each another, the electric field induces an electric polarization in a dielectric crystal, and the light itself is influenced by the crystal [9]. The frequency of light is in the range of 10^{14}–10^{15} Hz so only the electronic polarization can follow the electric field modulation [34].

Refractive index n is defined as the ratio of the speed of light in vacuum c_0 and in dielectric media c

$$n = \frac{c_0}{c} = \sqrt{\varepsilon_r} \,. \tag{2}$$

Typical refractive index values are between 2 and 2.5 in electro-optic crystals [35]. When an external electric field is applied to a ferroelectric crystal, ion displacement is induced and the refractive index is changed [36, 37]. The linear

shift of the refractive index under external electric field E is called the Pockels effect and can be expressed as [38]

$$\Delta n = \frac{1}{2} n^3 rE \,, \tag{3}$$

where r is the first order electro-optic coefficient. Correspondingly, second order electro-optic effect (Kerr effect) is described by

$$\Delta n = \frac{1}{2} n^3 RE^2 \,, \tag{4}$$

where R is the second order electro-optic coefficient.

Microscopically ferroelectrics are non-isotropic due to the internal polarization resulting in direction depended refractive index. The light propagation characteristics in anisotropic media can be described by index ellipsoid defined as [35]

$$\left(\frac{1}{n_x^2}\right)x^2 + \left(\frac{1}{n_y^2}\right)y^2 + \left(\frac{1}{n_z^2}\right)z^2 = 1 \,, \tag{5}$$

where the directions x, y and z are along the unit cells axes. As shown in Figure 2, 90° rotation of the BTO crystal around the polarization direction (z-axis) leaves the crystal invariant in the case of the ferroelectric structure due to tetragonal phase. Therefore, the crystal structure is uniaxial with refractive indices n_x=n_y=n_o and n_z=n_e . The index ellipsoid is then written as

$$\left(\frac{1}{n_o^2}\right)x^2 + \left(\frac{1}{n_o^2}\right)y^2 + \left(\frac{1}{n_e^2}\right)z^2 = 1 \tag{6}$$

and it is illustrated in Figure 5. At room temperature, the BTO lattice constants are 4.038 Å and 3.994 Å along and perpendicular to the polarization vector (P_s) direction, respectively [25]. The most dense directions in crystals have the highest refractive index [39] resulting in the smaller refractive index n_e=2.360 along the elongated unit cell direction and n_o=2.412 perpendicular to the polarization direction [40].

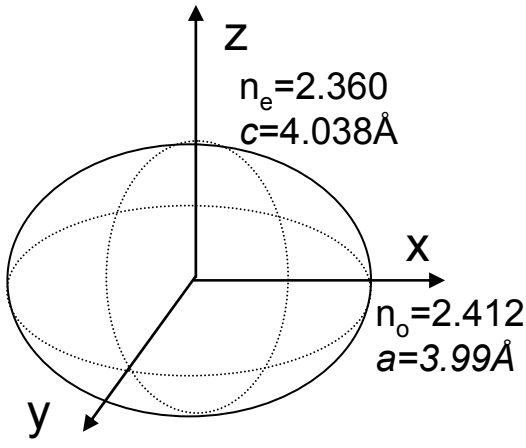

Figure 5. index ellipsoid of tetragonally distorted ferroelectric $BaTiO_3$ single crystal.

Under applied electric field the index ellipsoid deforms having the form [35]

$$\left(\frac{1}{n^2}\right)_1 x^2 + \left(\frac{1}{n^2}\right)_2 y^2 + \left(\frac{1}{n^2}\right)_3 z^2 + 2\left(\frac{1}{n^2}\right)_4 yz + 2\left(\frac{1}{n^2}\right)_5 xz + 2\left(\frac{1}{n^2}\right)_6 xy = 1 \quad (7)$$

with linear changes in the coefficients due to the electric field E defined by

$$\Delta\left(\frac{1}{n^2}\right)_i = r_{ij} E_j \,, \quad (8)$$

where E_j describes the electric field components with $E_1=E_x$, $E_2=E_y$ and $E_3=E_z$. The r_{ij} is called electro-optic tensor. Nonvanishing r_{ij}-element*s* of tetragonal BTO are $r_{13}=r_{23}$, r_{33} and $r_{42}=r_{51}$ [35, 41, 42]. The shifts of the index ellipsoid coefficients are obtained from the equation

$$\begin{vmatrix} \Delta\left(\frac{1}{n^2}\right)_1 \\ \Delta\left(\frac{1}{n^2}\right)_2 \\ \Delta\left(\frac{1}{n^2}\right)_3 \\ \Delta\left(\frac{1}{n^2}\right)_4 \\ \Delta\left(\frac{1}{n^2}\right)_5 \\ \Delta\left(\frac{1}{n^2}\right)_6 \end{vmatrix} = \begin{vmatrix} - & - & r_{13} \\ - & - & r_{13} \\ - & - & r_{33} \\ - & r_{42} & - \\ r_{42} & - & - \\ - & - & - \end{vmatrix} \begin{vmatrix} E_x \\ E_y \\ E_z \end{vmatrix} \tag{9}$$

and the index ellipsoid is described by the equation

$$\left(\frac{1}{n_o^2}+r_{13}E_z\right)x^2+\left(\frac{1}{n_o^2}+r_{13}E_z\right)y^2+\left(\frac{1}{n_e^2}+r_{33}E_z\right)z^2+2r_{42}E_y yz+2r_{42}E_x xz=1. \tag{10}$$

If the electric field is applied along the polarization direction ($E_z \neq 0$, $E_x=E_y=0$) the equation has the form

$$\left(\frac{1}{n_o^2}+r_{13}E_z\right)x^2+\left(\frac{1}{n_o^2}+r_{13}E_z\right)y^2+\left(\frac{1}{n_e^2}+r_{33}E_z\right)z^2=1\ . \tag{11}$$

By using the approximation [38, 41]

$$\Delta n=-\frac{n^3}{2}\Delta(\frac{1}{n^2})\,, \tag{12}$$

new expressions for the index of refraction along the principal directions are [41]

$$n_o^{'}=n_o-\frac{n_o^3}{2}r_{13}E_z \tag{13}$$

$$n_e^{'} = n_e - \frac{n_e^3}{2} r_{33} E_z \tag{14}$$

in accordance with the form of Expression (3) for the linear Pockels effect. Schematically the deformation of the index ellipsoid is illustrated in Figure 6(a). In the case of perpendicular electric field ($E_x \neq 0, E_z = E_y = 0$), the equation of the index ellipsoid has the form of

$$\left(\frac{1}{n_o^2}\right)x^2 + \left(\frac{1}{n_o^2}\right)y^2 + \left(\frac{1}{n_e^2}\right)z^2 + 2r_{42}E_x xz = 1 \tag{15}$$

with non-zero *xz*-element. The index ellipsoid is rotated around the *y* axis by an angle α [41]

$$\tan 2\alpha = \frac{2r_{42}E_x}{\frac{1}{n_o^2} - \frac{1}{n_e^2}} \tag{16}$$

with new index values

$$n_x^{'} = n_o - \frac{1}{2} n_o^3 r_{42} E_x \tan\alpha \tag{17}$$

$$n_z^{'} = n_e + \frac{1}{2} n_e^3 r_{42} E_x \tan\alpha \,. \tag{18}$$

The rotation of the index ellipsoid due to the electric field perpendicular to the polarization direction is illustrated in Figure 6(b). In Ref. [41], Expressions (17) and (18) were approximated at low field to have the forms

$$n_x^{'} \cong n_o - \frac{1}{2} n_o^3 (r_{42}E_x)^2 \frac{n_e^2 n_o^2}{n_e^2 - n_o^2} \tag{19}$$

$$n_z^{'} \cong n_o + \frac{1}{2} n_o^3 (r_{42}E_x)^2 \frac{n_e^2 n_o^2}{n_e^2 - n_o^2} \,. \tag{20}$$

An important consequence is the second order response in respect to the electric field strength in Equations (19) and (20).

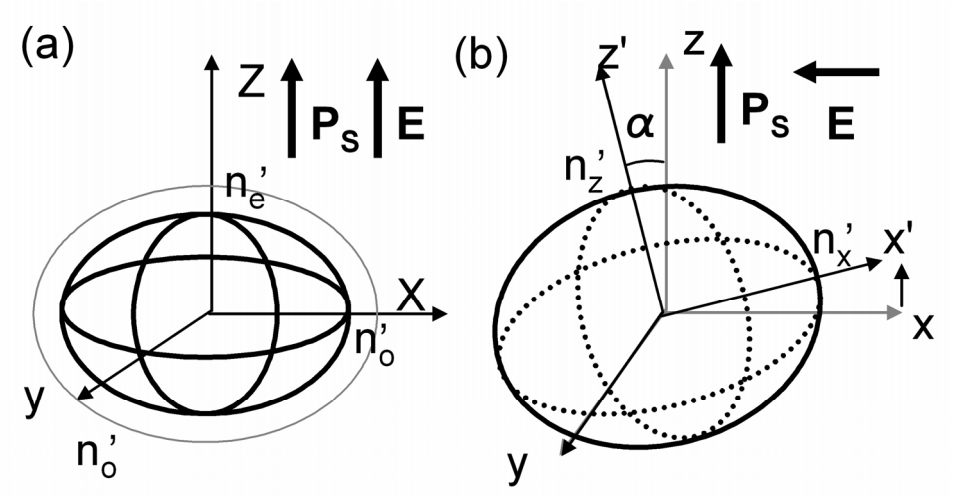

Figure 6. The deformation of the index ellipsoid of ferroelectric tetragonal $BaTiO_3$ in two cases, where applied electric field is (a) along the polarization direction and (b) perpendicular to the polarization direction.

The implications of Expressions (14)–(20) are now illustrated in the Mach-Zehnder intensity modulator device based on the bulk BTO single crystal. The device configurations are shown in Figure 7. Under an applied electric field, the phase shift is induced between beams propagating in different Mach-Zehnder arms, and the intensity at the output varies as a function of applied voltage. Figure 7(a) shows the device configuration, where the external electric field is along the spontaneous polarization vector direction corresponding to the situation in Figure 6(a). Figure 7(b) represents the arrangement, where the electric field is perpendicular to the polarization vector and the index ellipsoid is deformed as shown in Figure 6(b).

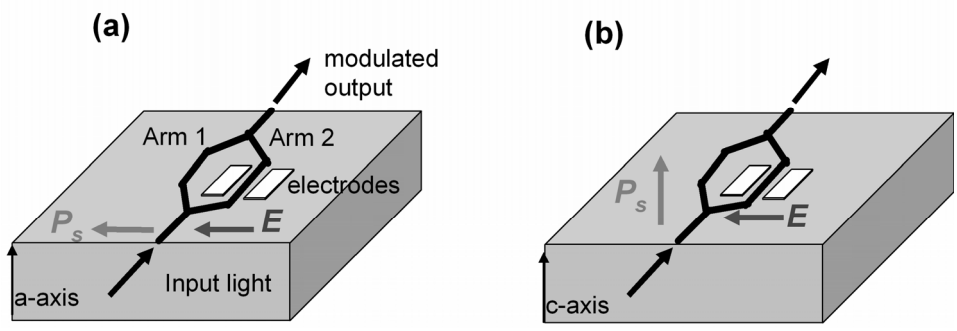

Figure 7. Mach-Zehnder modulator devices based on the BTO single crystal, where external electric field is (a) along and (b) perpendicular to the polarization vector P_S.

Calculations based on the Jones matrix have been used to evaluate the device operation [43]. J_{arm1} and J_{arm2} are defined as Jones matrices describing the shift in phase and polarization state of the light when transmitted through the two different arms. Arm 2 is denoted as the active arm between electrodes Figure 7. After the interference of two beams with Jones vectors J_1 and J_2, the output Jones vector is [42, 44]

$$J = J_{arm1} J_{in} + J_{arm2} J_{in} = J_1 + J_2 = \begin{pmatrix} A_{TE} \\ A_{TM} \end{pmatrix}. \tag{21}$$

J_{in} describes the Jones vectors of the input light and A_{TE} and A_{TM} describes the amplitudes of the two orthogonal polarization states of the output light. The output intensity is

$$I = \left|A_{TE}\right|^2 + \left|A_{TM}\right|^2. \tag{22}$$

Assuming TE-polarized light, the input polarization state is described as

$$J_{in} = \begin{pmatrix} 1 \\ 0 \end{pmatrix}. \tag{23}$$

If the external electric field E is along the direction of the polarization vector P_S in BTO, as shown in Figure 7(a), the rotation of the index ellipsoid does not occur, and the device operation can be evaluated by analyzing the effect of the phase difference between two arms according to

$$J_1 = \begin{pmatrix} 1 \\ 0 \end{pmatrix}$$
$$J_2 = \begin{pmatrix} e^{-j\varphi} \\ 0 \end{pmatrix} . \tag{24}$$

By summing J_1 and J_2 the output Jones vector is

$$J = \begin{pmatrix} 1 + e^{-j\varphi} \\ 0 \end{pmatrix} \tag{25}$$

from two interfering light beams with the same polarization state, and the intensity (22) now has the form [45]

$$I = I_0 \cos^2(\frac{\varphi}{2}) \tag{26}$$

with phase retardation difference φ due to the electro-optic effect in the arm 2. According to Expression (14):

$$\varphi = \frac{2\pi}{\lambda} * \frac{1}{2} n_e^3 r_{33} E * l , \tag{27}$$

where l is the length of the active arm in the Mach-Zehnder device.

Now, the situation in Figure 7(b) is analyzed. As mentioned above, external electric field perpendicular to the polarization vector rotates the index ellipsoid. J_1 is defined in the case of TE-polarized light as:

$$J_1 = \begin{pmatrix} e^{-jn_o \frac{2\pi}{\lambda} l} \\ 0 \end{pmatrix} \tag{28}$$

while J_2 includes now both the shift and rotation of the index ellipsoid:

$$J_2 = T(-\alpha) W T(\alpha) J_0 , \tag{29}$$

where

$$W = \begin{pmatrix} e^{-jn_x' \frac{2\pi}{\lambda} l} & 0 \\ 0 & e^{-jn_z' \frac{2\pi}{\lambda} l} \end{pmatrix} \tag{30}$$

includes the phase retardation in both TE and TM polarization directions. Rotations of the principal axis are taken into account by the rotation matrix

$$T(\alpha) = \begin{pmatrix} \cos\alpha & \sin\alpha \\ -\sin\alpha & \cos\alpha \end{pmatrix}. \tag{31}$$

Modified refractive indices in (30) are obtained from Equations (17) and (18) and the rotation angle of the principal axis from Equation (16). The results are illustrated in Figure 8 by using values in Ref. [41] for the single crystal BTO (r_{33}=23 pm/V, r_{42}=820 pm/V), wavelength λ=1550 nm and by using the arm length of 10 mm. The shifts of the indices as a function of electric field are plotted in Figure 8(a) in two cases, where the electric field is along and perpendicular to the polarization vector. It is important to note that though r_{42} has a high value of 820 pm/V, its influence is dependent on the initial values of n_o and n_e. Therefore, values of effective electro-optic coefficients in Expressions (3) and (4) are commonly used to describe the observed net effect instead of the tensor elements [18]. Figure 8(b) shows the intensity modulation of the Mach-Zehnder device as a function of electric field according to Equation (26) in the case of parallel electric field and polarization directions. The linear shift of the refractive index produces, naturally, periodically oscillating intensity as a function of electric field. Correspondingly, Figure 8(c) illustrates the intensity modulation in the cases, where electric field and spontaneous polarization are orthogonal (Figure 7(b)). The values are obtained from Equation (22) and applying Expressions (28) and (29). The non-linear shift in the refractive index produces now intensity oscillation with decreasing periodicity as a function of electric field. The rotation of the principal axis, see Equation (16), at the electric field of 1 V/μm is about 6° producing only a low decrease in modulation depth. Therefore, the rotation of the index ellipsoid can be neglected when approximating the device operation [44]. Now, the phase shift method used in the first case (Equations (24)–(26)) can be used with the phase difference

$$\varphi = \frac{2\pi}{\lambda} * \frac{1}{2} n_o^3 r_{42} E \tan\alpha * l, \tag{32}$$

where the index shift is obtained from Expression (17).

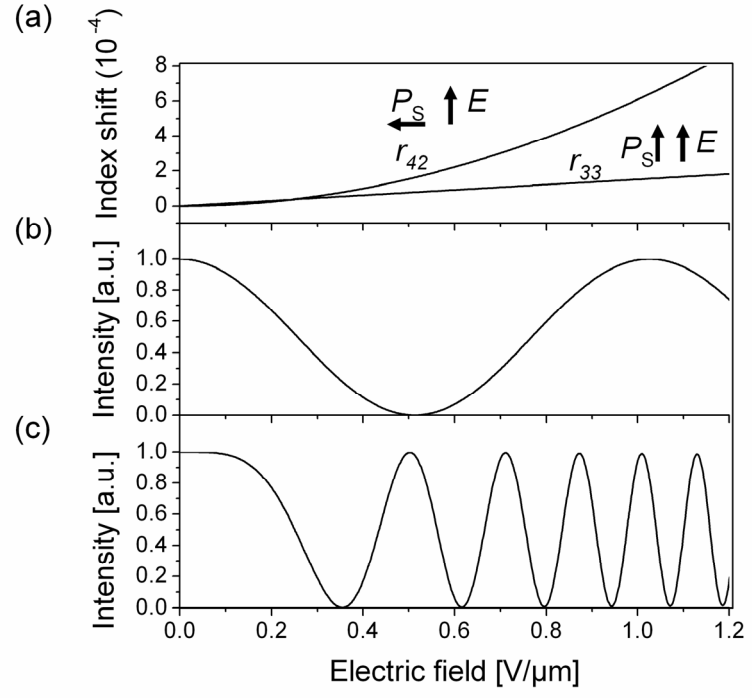

Figure 8. (a) Shift of the refractive index in BTO single crystal, when an electric field is applied along and perpendicular to polarization vector. Electro-optic modulation in the Mach-Zehnder device when the electric field is along the polarization vector (b) and perpendicular to the polarization vector (c).

The approach described above applies to well defined bulk crystals. The situation in thin films with not so well defined polarization vector orientation and with stress effects induced from the substrate on the crystal structure may be such that electro-optic modulation is induced in both directions and the measured net response can be a combination of the first and second order responses though the origin of the activity is the Pockels effect [46]. Furthermore, in polydomain structures electric field can induce also domain reorientation that can contribute in addition to the non-linearity in the EO effect.

3. Studied microstructures

3.1 Polycrystalline $Pb(Zr_xTi_{1-x})O_3$ thin films

$Pb(Zr_xTi_{1-x})O_3$ (PZT) ceramics posses several phases including paraelectric, ferroelectric and antiferroelectric phases depending on the temperature and Zr-Ti ratio. Technologically, the most interesting composition range is $0.49<x<0.64$. The morphotropic phase boundary (MPB) locates within this region with ferroelectric tetragonal phase at Ti rich compositions and ferroelectric rhomboedral phases at Zr rich compositions [22]. At compositions near the MPB physical parameters such as dielectric constant, piezoelectric constant and electro-optic coefficient reach their maximum values. Electrical, electromechanical and optical properties of PZT offer a wide variety of applications in microsystems. A strong electro-optic response together with optical transmittance of PZT thin films can be utilized in functional optical applications [17]. The modification of PZT ceramics with different elements like La and Nd further improves the properties of the ceramics. For example, La-modified PZT ceramics (PLZT) have been reported to have excellent optical properties also in the form of thin films and they are utilized, in a lot of different applications like in acousto-optic deflectors [17].

Grain size effects in ferroelectric ceramics give an important ability to influence the physical properties [47, 48]. In the case of thin films on different substrates and having also different film thicknesses, their optical properties are greatly affected by crystal structure, orientation of crystals, grain size distribution, packing density, and morphology of the film surface. Some of these factors depend strongly on the deposition of the films and on thermal heat-treatment processes. In the case of polycrystalline PZT films grown by PLD, the films are typically composed of nanograins. In this work, the influence of the heat-treatment process on the grain size and subsequently on the optical properties of the Nd-modified PZT thin films was studied. Especially, the dependence of refractive index and electro-optic response was investigated as a function of grain size distribution. Characterized PZT films were deposited from a Nd-modified PZT target by using PLD process. The effect of Nd-addition on the properties of PZT is comparable to that of La-addition [49].

3.2 Epitaxial and nearly epitaxial $BaTiO_3$ thin films

Many values of the vital physical properties of BTO films commonly differ from bulk values, being often degraded, but in some cases even enhanced, such as the increased remanent polarization in strained BTO films due to substrate induced stress [50]. Both experimental and theoretical studies suggest that significant increases in phase transition Curie temperature may result from strains induced by lattice mismatch or from differences between the coefficients of the thermal expansion of epitaxial film and substrate [50–58]. Furthermore, theoretical studies [52, 55–57] suggest that the room temperature phase need not necessarily be tetragonal as is the case in the bulk sample, but also other phases are possible, depending on the amount of stress and its character, i.e., tensile or compressive.

One demonstrated possibility to modify the lattice parameters of perovskite thin films is to vary the oxygen working pressure during the film growth [59–65]. Several mechanisms have been suggested to influence the changes in crystal structure and in values of lattice constants, such as lattice mismatch [50, 66], difference of thermal expansion coefficients between the substrate and film [67, 68] and deviation in both stoichiometry [60, 64] and deposition kinetics [59]. When epitaxial thin films are deposited on near lattice-matched substrates large intrinsic strains may be created since the film lattice attempts to follow the substrate lattice periodicity. As a result, strain-induced structural changes can have a significant effect on the film properties. The lattice constant of cubic MgO is 4.21 Å [69] and for tetragonal BTO lattice constants have the values c=4.038 Å and a=3.994 Å [25]. This would lead to tensile stress in an epitaxial BTO film on MgO. On the other hand, strain due to the thermal expansion difference between the film and substrate also affects the structure of the deposited film during cooling from the deposition temperature down to room temperature. For example, it was estimated that during the cooling process from a typical deposition temperature of 700 °C to room temperature, the parallel to substrate surface strain is –0.28% between BTO film and MgO substrate [68]. This may create a compressive stress for in-plane directions in BTO film favoring a condition where the c axis of the BTO in the tetragonal phase aligns itself parallel to the surface normal [67, 68].

The lattice of an oxygen deficient perovskite film expands beyond that of the corresponding bulk ceramic [64] as a result of the shifted nearest neighbor

distance, due to the reduced Coulomb attractive force between cations and anions in an oxygen deficient lattice. Oxygen vacancies are also proposed as a mechanism which affect the internal stress state change in perovskites (from compressive to tensile with increasing oxygen pressure). As a result of the shift in lattice parameter mismatch between the film and substrate, the stress state can be changed. This can result in a change in the preferred orientation of the film [59, 60, 62, 64, 65] and even in the crystal structure, e.g., between the paraelectric and ferroelectric phases, depending on the working pressure [70].

The control of oxygen partial pressure during the film growth by PLD has been shown to be a means for tuning the structure and dielectric properties of perovskite thin films. Since BTO has been demonstrated as a potential material choice in optical waveguide modulators with promising electro-optic responses [42, 71], our motivation was to study the influence of oxygen partial pressure during BTO film deposition on the physical properties of the films which are important for the realization of electro-optic waveguide devices.

3.3 Ferroelectric-paraelectric superlattices

Research efforts have been focused on attempts to improve the properties of BTO thin films, mostly permittivity, by the formation of solid solutions and multilayer structures with $SrTiO_3$ (STO). For example in $Ba_xSr_{1-x}TiO_3$ (BST) solid solutions, the tunability of the permittivity can be up to 80% [72]. Another approach is to deposit alternating layers of these materials to form composite superlattice structures with unique properties [73]. Interestingly, their physical properties can be quite different from those in compositionally equivalent solid solutions. In the case of oxide superlattices of BTO and STO, stacking structure has been shown to be an important parameter to engineer permittivity and its nonlinearity with tunability values as high as 94% in the optimized structure [74, 75].

These superlattices have been fabricated with a very accurate control of the stacking periodicity, down to the order of a unit cell length, by different methods like molecular beam epitaxy (MBE) and pulsed laser deposition (PLD) [74, 76]. Relatively large stresses are induced in such superlattice structures due to the mismatch between the stress-free in-plane lattice parameters of 3.994 Å and

3.905 Å for BTO [25] and STO [77] respectively. Stresses are relaxed by the formation of dislocations, the density and distribution of which depend on the thickness of the film. As a result, strain can be controlled by adjusting the layer thicknesses of the superlattice [73]. Besides the mechanical coupling, another factor affecting the dielectric properties is the electrostatic coupling between the ferroelectric and paraelectric layers, when a polarized ferroelectric layer tends to induce dipoles also in paraelectric materials [78, 79].

While the majority of research on oxide superlattices has been focused on the dielectric properties, significant enhancements in second-harmonic generation upon optimization of the stacking periodicity in BTO-STO superlattices [80] have been observed. This technique has also been utilized to study the internal dipole structure of these composite structures [81]. Likewise, enhancements in the electro-optic response in relaxor oxide superlattice structures have been reported [82]. The aim in this work was to study whether BTO-STO based superlattices can be used to produce structures with high electro-optic coefficients in the same method that the tunability of the permittivity could be enhanced by the use of superlattices.

4. Experimental

4.1 Pulsed laser deposition of thin films

All the thin films in this work were deposited by pulsed laser deposition (PLD). In PLD, high intensity laser pulses are absorbed by the target material, causing the evaporation and the ablation of atoms, ions and clusters forming a thin plasma layer on the surface of the target [14]. During the laser pulse exposure, the emitted particles absorb energy from the laser beam, resulting in plasma that expands in a perpendicular direction to the target surface, and can be collected onto a substrate.

In the case of crystalline oxide materials, the film growth can be carried out mainly by two methods [14, 49]. Substrate heating is utilized during 1) *in-situ* process with typical temperatures between 400–1000 °C and an oxygen gas working atmosphere leading to a direct crystallization of the ablated species reaching the substrate surface. Deposition can be made also in a vacuum without substrate heating. In this case amorphous as-deposited films can be crystallized with 2) a *post-annealing* treatment. Both in-situ and post-annealing techniques were applied in this work to produce different types of microstructures. When a nearly lattice-matched material is grown in-situ on the substrate, typically high growth of highly preferred crystal orientation (epitaxial or nearly epitaxial) occurs. A post-annealing technique produces polycrystalline samples as a result of randomly distributed nucleation centers. The final microstructure of the film is commonly very sensitive to processing conditions. This property is applied during this work in the manufacture of the thin films.

Two different deposition systems were used in this work. The main difference between these systems was the used excimer laser wavelength. The other system was equipped with XeCl laser (located at the University of Oulu) operating at a wavelength of 308 nm and the other laser system (located at Massachusetts Institute of Technology) with KrF 246 nm wavelength laser.

4.1.1 Polycrystalline $Pb(Zr,Ti)O_3$ thin films

The pulsed XeCl-excimer laser and $Pb_{0.97}Nd_{0.02}(Zr_{0.55}Ti_{0.45})O_3$ target were used to deposit amorphous Nd-modified lead-zirconate-titanate (PNZT) thin films on MgO(100) substrate. The deposition was carried out without substrate heating at room temperature at a pressure of 6×10^{-5} mbar. In order to achieve films with different grain size distribution, the PNZT thin films were annealed at 700 ºC, 800 ºC and 900 °C, respectively, for 20 minutes under an inverted zirconia crucible together with some PNZT powder after the deposition. The same heating and cooling rate of 400 °C/h was used in every temperature profile.

4.1.2 Highly oriented $BaTiO_3$ thin films

Highly oriented BTO thin films were grown onto single crystal MgO(001) substrates. The deposition system was equipped with a KrF (248 nm) excimer laser, with its beam focused onto the nominally stoichiometric BTO pressed and sintered target. All films were grown by using a laser repetition rate of 5 Hz. The substrates were heated up to 700 °C at a rate of 10 °C/min before deposition with oxygen partial pressure being the only varied process parameter. Oxygen pressures of 1.5, 10, 15, 20, 25 and 30 mTorr (2×10^{-3}, 1.3×10^{-2}, 2×10^{-2}, 2.7×10^{-2}, 3.3×10^{-2} or 4×10^{-2} mbar) were used respectively, during depositions and the samples were cooled down to room temperature at a rate of 5 °C/min.

4.1.3 $BaTiO_3$–$SrTiO_3$ superlattices

$BaTiO_3$–$SrTiO_3$ thin-film stacks with periodicity between 27 and 1670 Å were deposited onto single crystal MgO(001) substrates by alternately focusing the laser beam on nominally stoichiometric BTO and STO targets. The thickness of each layer was controlled by tracking the number of laser pulses during the deposition with known deposition rates. In the study that was published in Paper IV, the deposition system equipped with XeCl laser was used to grow the BTO-STO stacks with varying stacking periodicity. A substrate temperature of 800 °C and total oxygen working pressure of $5*10^{-3}$ mbar were maintained during the deposition. At first, a BTO seed layer with thickness of 20 nm was grown on the

substrate followed by the periodic pairs of BTO-STO layers with a total film thickness of about 360 nm.

The BTO-STO superlattices used in the modulator devices (Paper V) were grown by KrF-laser setup. A substrate temperature of 700 °C and total oxygen working pressure of 15 mTorr were maintained during deposition. A BTO interfacial layer with thickness of 30 nm was grown on the substrate before the deposition of BTO-STO layers with a total film thickness of 180 nm.

4.2 X-ray diffraction studies

The crystal structure of the thin films was examined by x-ray diffraction (XRD) measurements. The crystal structures, grain size distributions and preferred orientations in films were characterized from θ-2θ scans. The mean grain size of polycrystalline PNZT films was calculated by using the Warren-Averbach method (WinFit software) [83].These scans were also utilized to calculate the out-of-plane lattice parameters of the BTO films. The MgO reflections were used as an internal reference to make 2θ corrections. When characteristic material reflections were observed, as it was the case with single layer BTO films and BTO-STO superlattices of long stacking periodicity, the lattice parameters were determined from fitted diffraction peaks (JADE and WinFit software). Non parallel-to-surface planes of BTO films were mapped (Bruker D8 equipment) to identify the symmetry of the crystal planes and to calculate the in-plane lattice parameter with the help of θ-2θ scan results.

The characteristic reflections of BTO and STO were not observed in the case of short periodicity superlattices, when out-of-plane lattice parameters were estimated by a simulation method taking into account angle dependent x-ray scattering factors of different ions in stacked perovskite structures and the Lorentz-polarization factor [84, 85]. In single layer BTO or STO film, the structure factor can be expressed as

$$F_{\mathrm{BTO/STO}} = \sum_j a(j) e^{iqz} , \qquad (33)$$

where *a(j)* are the atomic (ionic) scattering factors and sum *j* runs over the ions in perovskite unit cell. The films were epitaxial/nearly epitaxial with (00m) orientation, so only the *z*-direction (out-of-plane) was included in calculation. In this expression the scattering vector length *q* is

$$q = 2\frac{2\pi}{\lambda}\sin(\theta)\,. \tag{34}$$

In superlattices the crystal periodicity is the length of the supercell, which consists of BTO and STO perovskite cells illustrated in Figure 9(a).

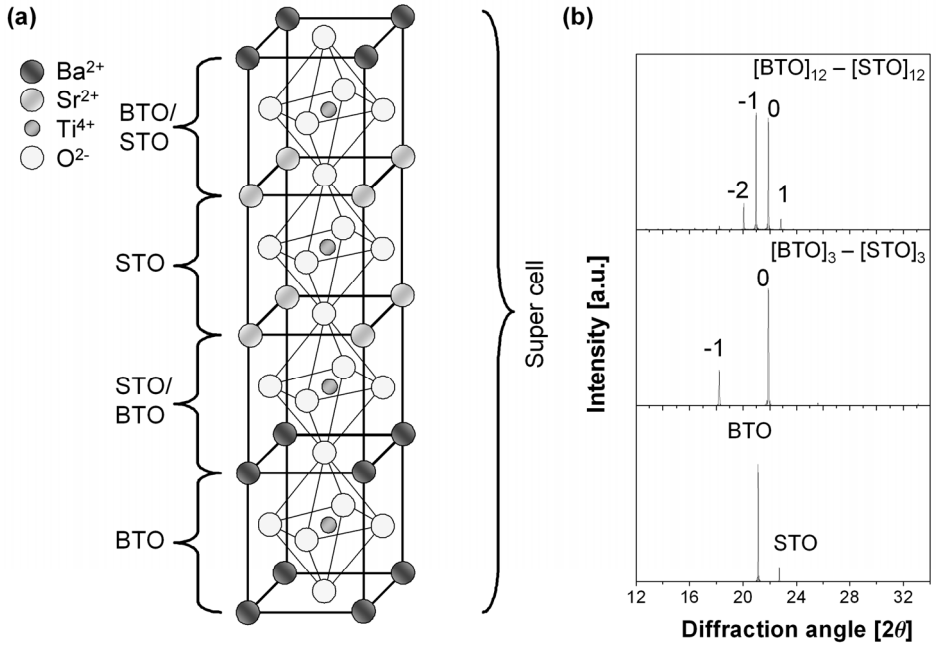

Figure 9. (a) The supercell structure in periodic BTO-STO superlattices. The lowest pattern in (b) represents the simulated XRD θ–2θ patterns of the superimposed BTO and STO single layer structures. Above is illustrated the formation of satellite reflections in superlattices with 3 and 12 unit cell periodicities, respectively.

The supercell structure factor is expressed now as

$$F_{\text{super cell}} = \sum F_{\text{BTO/STO}} e^{iqd_{\text{BTO/STO}}} , \qquad (35)$$

where the summation consists of the phase modified BTO and STO structure factors $F_{\text{BTO/ STO}}$. The perovskite cell length $d_{\text{BTO/STO}}$ is along the out-of-plane direction. Figure 9(b) illustrates the influence of the stacking periodicity on the XRD θ-2θ patterns. The lowest plot presents the superimposed BTO and STO simulation patterns with characteristic (001) materials reflections. In two upper plots are shown the simulated curves of the BTO-STO superlattices with periodicities of 3 and 12 unit cells. The characteristic BTO and STO diffraction peaks are now replaced by the bundle of the superlattice reflections with the number on the peaks representing the order of the satellite reflections. The periodicity of the satellite reflections depends on the stacking structure with increasing angle spacing with decreasing stacking periodicity according to the Bragg equation.

4.3 Dielectric properties

A micro-probe station, equipped with an HP 4192A impedance analyzer, was utilized in the dielectric measurements. Relative permittivity and its tunability, i.e. change in permittivity as a function of applied bias electric field, were characterized with a platinum inter-digital-electrode (IDE) configuration, which was sputter deposited onto the film and lift-off patterned.

The error in permittivity due to the geometrical variation of electrodes was estimated by fabricating IDE capacitors with 10 μm (52 fingers) and 20 μm (26 fingers) widths and separation and length of 800 μm. By using Farnell's analysis [86] and applying a stray circuit model to take into account a finite impedance of cables, probes and electrodes, less than 9% deviation was observed in permittivity between different electrode configurations on the same film. Prior to dielectric measurements, the electroded samples were heated up to 500 °C and cooled down to room temperature to avoid potential electrode destabilization effects during actual measurements. The sample temperature was monitored by a thermocouple attached to the sample during elevated temperature permittivity studies.

4.4 Waveguide fabrication

To confirm the suitability of the BTO single layer and BTO-STO multilayer structures in optical guided wave devices and to characterize the electro-optical properties, Mach-Zehnder waveguide intensity modulator structures were fabricated. Recently, directly etched ridge [42, 87] and strip-loaded [18] type optical waveguide structures based on ferroelectric thin film technology have been demonstrated. A strip-loaded type device was chosen, since this allows for the use of easily patterned materials for the guiding structure rather than having to pattern the superlattice stack itself. A fabricated structure on a MgO substrate (n=1.70) is shown in Figure 10. Si_xN_y layers with thickness of 270 nm were grown by plasma enhanced chemical vapor deposition (PECVD) and lithographically patterned and etched by reactive ion etching (RIE). A refractive index of 1.79 was measured at 1550 nm wavelength for a Si_xN_y slab film prepared in the same manner as the above Si_xN_y layer. Al electrodes adjacent to the active arm were sputter deposited and lithographically patterned and etched with standard aluminum wet etchant.

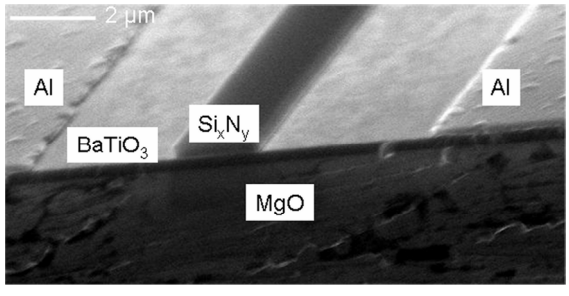

Figure 10. Cross section scanning-electron-microscope image of the active arm of the Mach-Zehnder modulator with Si_xN_y strip-loaded waveguide structure on $BaTiO_3$ thin film.

By using the expression [71]

$$r_{eff} = \frac{\lambda\, g}{n^3 L\, V_\pi \Gamma} \tag{36}$$

the values of effective linear electro-optic coefficient r_{eff} can be extracted. The electrode length L and the separation g between the electrodes were 3 mm and 9–15 µm, respectively. V_π is the voltage required to cause a 180° phase shift. Γ is

an overlap factor describing the portion of the light in the active layer experiencing the electro-optic effect and was obtained by using a commercial simulation software (FIMMWAVE). The induced electric field was assumed to be homogenous in the vicinity of the guiding Si_xN_y strip due to relatively large electrode separation, and this was also supported by simulations (COMSOL MULTIPHYSICS). The thicknesses of the active films in this work were between 180 nm (Paper V) and ~400 nm (Paper III) with estimated values of the overlap factor between 0.39 and 0.74, respectively.

4.5 Characterization of optical properties

The refractive index *n* and extinction coefficient *k* of the polycrystalline PNZT films were determined by spectral UV-VIS-NIR transmission method [Paper I]. SCI Film Spectrum software was utilized to fit *n* and *k* with measured data. An example of this kind of measurement data is shown in Figure 11(a). The relative high modulation in transmittance is due to the high refractive index contrast between the film (2.25–2.5) and substrate ~1.7–1.72.

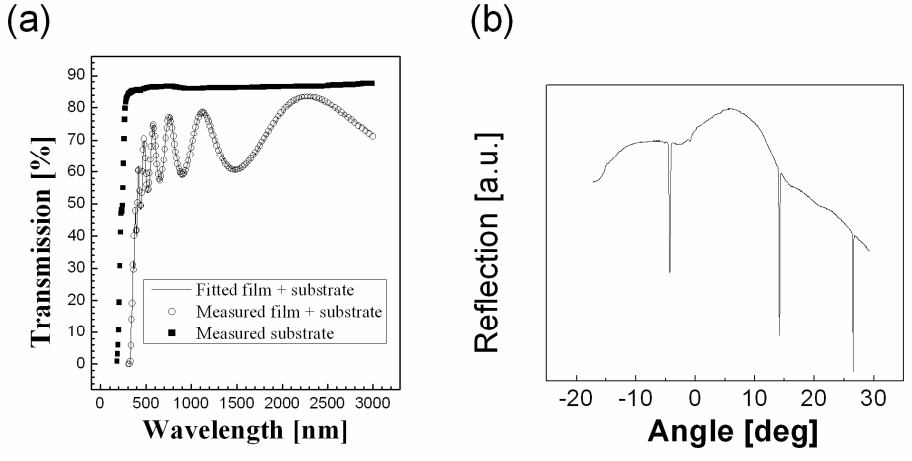

Figure 11. Transmission (a) and prism-coupling (b) methods used in this work to characterize the static optical properties of the films.

Refractive indices of single layer BTO films and BTO-STO superlattices were measured by the prism coupling method (Metricon 2010) [88, 89]. The setup

was equipped with a polarization state shifter allowing the determination of refractive indices along both in-plane and out-of-plane directions. Figure 11(b) illustrates a typical result of the prism coupling measurement of an epitaxial BTO film. In this measurement, the thin film sample is pressed against a high index prism. A laser sourced beam is directed towards the base of the rotating prism, and normally the beam experiences a total internal reflection due to index contrast between the prism and the sample. However, at certain discrete incident angles, light couples via an evanescent field into the film as a guided optical mode, resulting in a sharp drop in the reflected intensity.

Electro-optic responses of the slab films were measured with a similar setup used, e.g., by Adachi *et al.* [90] and illustrated in Figure 12(a). In order to study the electro-optic response evolution with increasing crystallite size in polycrystalline PNZT films and with stacking periodicity of the BTO-STO films, Cr electrodes were deposited on the top of the film by using e-beam evaporation with physical masking. In this arrangement an He-Ne laser (633 nm) sourced beam was directed into the gap between electrodes. The polarization state angle of the incoming beam was at 45° relative to the applied electric field direction. In-plane induced shift in birefringence $\delta\Delta n$ due to electro-optic effect causes the phase retardation φ between perpendicular field components and can be expressed as

$$\varphi = \frac{2\pi}{\lambda}\delta\Delta n d \,, \tag{37}$$

where λ is the wavelength and d the film thickness. By using a quarter wave plate the polarization state is returned back to linear, but with slightly different angle α from 45° and this shift was measured. The phase retardation shift φ due electro-optic effect can be obtained by doubling the polarization angle shift in this measurement arrangement [90]. The setup was equipped with a polarization splitting prism and the polarization angle was determined by measuring the intensity difference between the orthogonal components $I_x=E_x^2=E^2\cos^2(\alpha)$ and $I_y=E_y^2=E^2\sin^2(\alpha)$ with two oppositely coupled photo detectors i.e. $I_x - I_y = E^2 [\cos^2(\alpha) - \sin^2(\alpha)] \rightarrow (I_x - I_y)/I = \cos(2\alpha)$. The setup was equipped with a phase lock amplifier that was frequency matched with a chopper modulating the laser light. Figure 12(b) illustrates a typical measurement result of the birefringence shift in PNZT as a function of applied electric field.

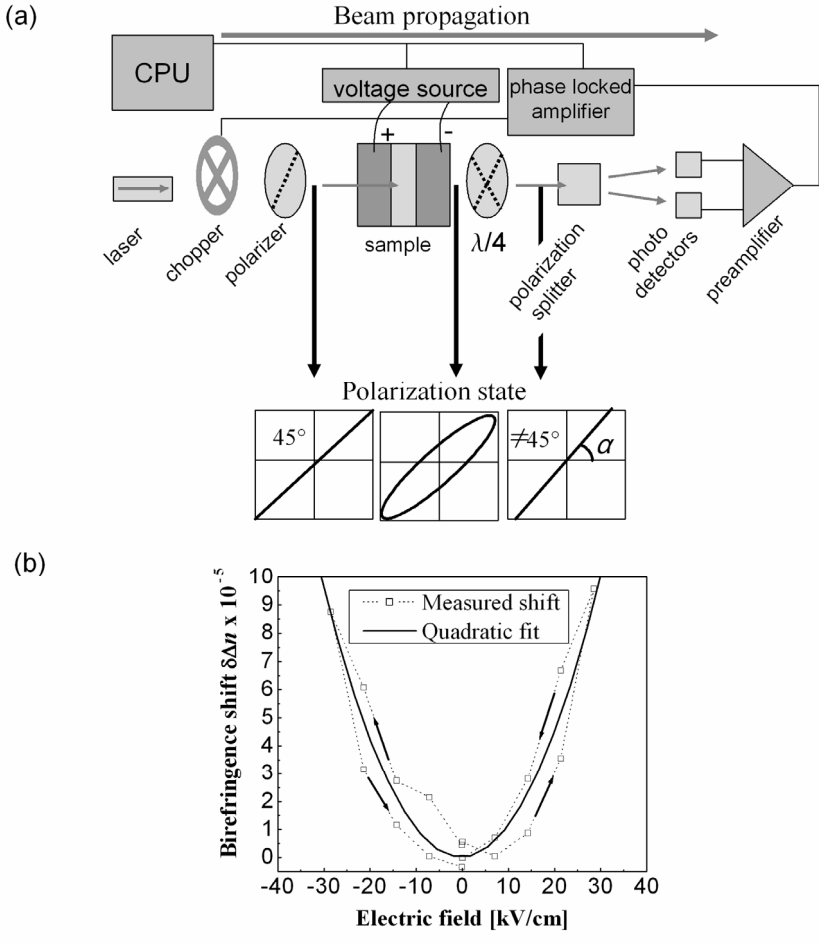

Figure 12. (a) The measurement setup used to characterize the electro-optic response in slab film and (b) a typical measurement result of birefringence shift as a function of applied electric field.

Figure 13(a) shows the measurement setup used to characterize the waveguide properties of BTO and BTO-STO based devices and Figure 13(b) and (c) show characterization results obtained with this arrangement. A fiber coupled laser operating at 1550 nm wavelength was used as a light source in the waveguide device measurements. The intensity was modulated with a chopper located between two free space optical fiber connectors. The measurement setup was also equipped with a fiber coupled polarization state controller. The correct polarization at the input fiber was confirmed with the external polarizator before

the actual waveguide measurement. TE polarized light was end-fire coupled into the Mach-Zehnder waveguide modulator from the lensed input fiber. Proper waveguide operation was verified by imaging the output intensity distribution with a microscope objective coupled infrared camera (see Figure 13(b)). During the electro-optic measurements, a voltage sweep was applied across the electrodes, and the microscope objective collected light was directed to an optical power meter instead of the camera. The intensity was read from a phase lock amplifier that was frequency matched with the chopper. Figure 13(c) illustrates the intensity variation during the voltage sweep. The observed intensity modulation depth varied between about 2 and 9 dB. The variation in modulation depth was assumed to be due to defects near the waveguides inducing scattering and non-ideal intensity splitting/coupling in the test structures.

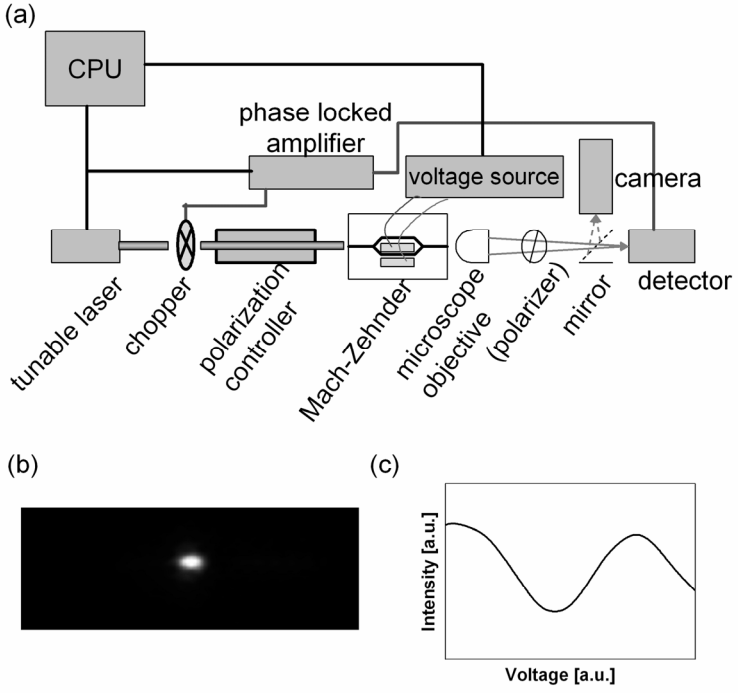

Figure 13. (a) The measurement setup used to characterize the Mach-Zehnder device waveguiding and electro-optic properties. In (b) and (c) are illustrated data obtained by using this setup: (b) intensity distribution at waveguide output facet and (c) intensity modulation as a function of applied voltage.

5. Results and discussion

5.1 Grain size effects in polycrystalline PNZT thin films

According to the XRD studies the mean grain size of $Pb_{0.97}Nd_{0.02}(Zr_{0.55}Ti_{0.45})O_3$ (PNZT) thin films varied between 91 and 213 Å with increasing post-annealing temperature from 700 ºC to 900 °C [Paper I]. Both refractive index and electro-optic coefficients were found to increase with increasing mean grain size, as is shown in Figure 14. The shift in birefringence followed nearly the second order response as shown in Figure 12(b) and Expression (4) was used to evaluate the strength of the electro-optic effect.

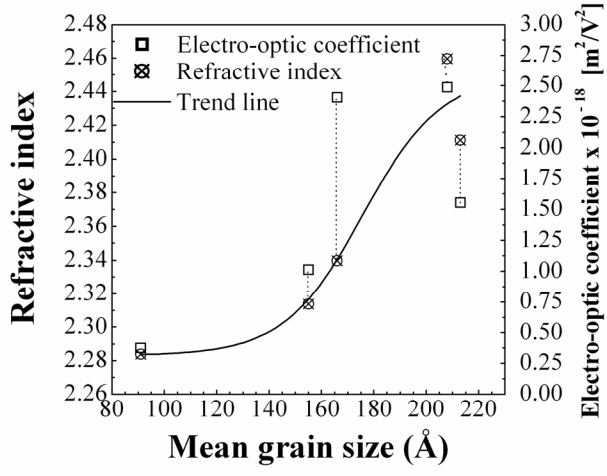

Figure 14. Refractive index n *and electro-optic coefficient* R *as a function of mean grain size of the PNZT thin films post-annealed at temperatures from 700 ºC to 900 ºC [Paper I].*

Values of the second order electro-optic coefficient *R* increase from 0.37×10^{-18} m^2/V^2 to $\sim2\times10^{-18}$ m^2/V^2 with increasing mean grain size in Figure 14. Corresponding birefringence shift spans now from 1.4×10^{-5} to 12×10^{-5} at the electric field of 25 kV/cm. These values of *R* are small compared to the electro-optic coefficient of relaxor PLZT (8.8/65/35) with the value of 8×10^{-16} m^2/V^2 for bulk ceramic [91] and for sputter prepared epitaxial PLZT thin films with

compositions of (9/65/35) and (28/0/100), values of $1.0\times10^{-16}m^2/V^2$ and 0.6×10^{-16} m^2/V^2 have been reported, respectively [17]. However, the values are comparable to the ones in sol-gel deposited PLZT films [92, 93]. Correspondingly, the value of the refractive index increased from 2.28 to above 2.45 with increasing mean grain size in Figure 14. In the films with mean grain size above 200 Å, the refractive index approaches typical bulk values of PZT with various compositions [94].

The critical crystallite size where the ferroelectric tetragonal phase transforms to paraelectric cubic phase in $PbTiO_3$ was estimated to be around 70 Å by Chattopadhyay *et al.* [95]. Experimental works suggest that the critical size can vary depending on the composition and stress [47]. $PbTiO_3$ thin films maintain ferroelectricity down to the film thickness of 7–14 nm. This size effect suppresses various properties like remanent polarization, dielectric constant and piezoelectric constants. Because the mean grain size of the films with weak electro-optic coefficients was found to be around 100 Å, a part of the grains is assumed to be already in the paraelectric cubic phase reducing thus the electro-optic effect. The cubic crystal structure can have an influence on the refractive index due to different unit cell structure. Furthermore, the volume occupied by the amorphous grain boundaries increases in the films with decreasing grain size. Since the total dielectric constant of the film is a combination of dielectric constants of grain boundaries and various crystallite phases, the electric field induced birefringence shift is assumed to be lower in films with smaller grains.

5.2 Highly oriented $BaTiO_3$ thin films

5.2.1 Lattice strains and orientation

Figure 15 shows the results of XRD θ-2θ measurements of BTO films on MgO(001) substrate deposited at different oxygen pressures [Paper II]. Only the (001) peak and its multiples are seen in the patterns from the thin films grown at oxygen pressures ≤10 mTorr. The diffraction peaks from the thin films shifted towards lower diffraction angles as compared to characteristic bulk BTO (00m) angles, implying an enlargement of the out-of-plane lattice parameter as compared to the corresponding bulk *c*-axis value. The main peaks shifted

between the characteristic bulk BTO (00m) and (m00) angles as the oxygen pressure was increased during deposition, indicating a change in preferred orientation from (001) to (100) orientation. When the oxygen pressure exceeded 15mTorr, reflections from (110)/(101) oriented planes were also seen in the θ-2θ patterns together with (m00) main peaks indicating a change from hetero epitaxial film to a polycrystalline structure. As the oxygen pressure reached 25 mTorr, minor non-characteristic tetragonal BTO phases were also observable in the θ-2θ pattern.

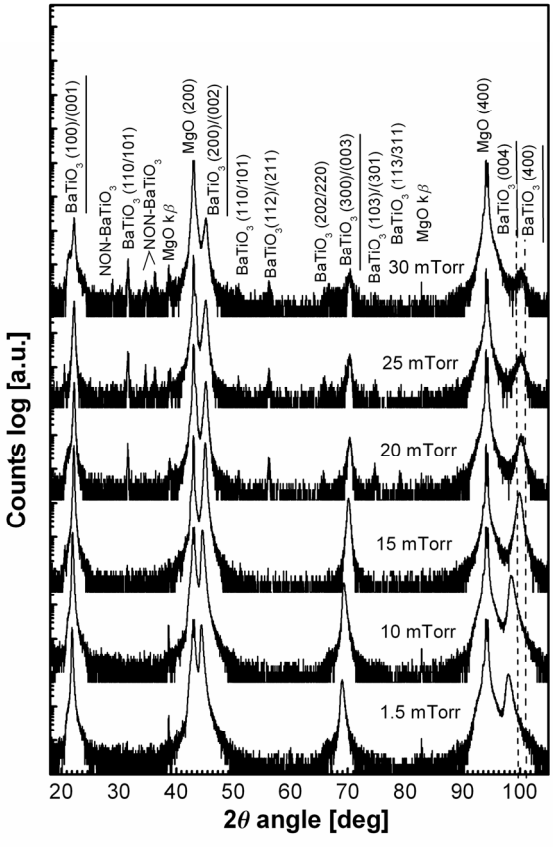

Figure 15. X-ray diffraction θ-2θ patterns of $BaTiO_3$ films deposited at different oxygen pressures. Dashed lines near 2θ = 100° represent bulk $BaTiO_3$ (004) and (400) reflections at room temperature. Underlined labels represent the (00m)/(m00) reflections, which are from the preferred orientation planes in $BaTiO_3$ films [Paper II].

The asymmetric peaks may imply non-uniform microstrains in the films. Analysis of $K\alpha_2$ radiation removed patterns revealed that, in films deposited at 1.5 and 10 mTorrs, the peaks are more spread to higher angles towards the characteristic c-axis peak position, possibly due to strain relaxation. The 15 mTorr sample has the most symmetric peaks, indicating uniform stress level. The peaks of films deposited at 20, 25 and 30 mTorrs are non-symmetrically spread towards the lower angle. Related strains have been also observed in PZT films experiencing $c \rightarrow a$ axis reorientation as a function of film thickness and having the highest level of microstrain in a-axis oriented films near the reorientation point and local minimum in microstrain on the *c*-side of the reorientation point [96].

The break down of epitaxy was observed also in rocking curve measurements of (002)/(200) reflections and φ-scan measurements of (103)/(301) planes when samples were rotated by 360° as shown in Paper II. FWHM value increased due to epitaxy break down in rocking curve measurements and in φ-scans each sample showed 4-fold symmetry along the MgO crystal direction. In the films deposited at low pressures $\leq$ 15 mTorr, the intensity between peaks was very low, further supporting the hetero-epitaxial film structure. The films were textured, when the oxygen pressure was 20 mTorr or higher. Peaks were broader and a slight intensity remained at all φ angles, presumably due to the randomly oriented grains between the substrate-aligned columns. For the 30 mTorr sample, the peaks became sharper, correlating with rocking curve measurements, and indicating a stronger influence of substrate on the crystal orientation of the film.

Figure 16 shows the evolution of the lattice parameters as a function of the oxygen pressure during film growth. As the gas pressure increases, the out-of-plane lattice constant decreases. At low oxygen pressures the lattice constant was significantly larger than that of the BTO single crystal *c*=4.038 Å [25]. The *c*-axis values of 4.09 Å and 4.07 Å were determined for the films deposited at the oxygen pressures of 1.5 and 10 mTorr, respectively. Epitaxial BTO films with *c*-axis orientation can possess a significantly strained out-of-plane axis from the bulk BTO value when grown on various substrates [50, 66]. It was also suggested that the in-plane lattice constant does not necessary differ remarkably from the corresponding bulk value with fluctuating out-of-plane parameter. This was also observed in this study in the samples deposited at low oxygen

pressures, where the in-plane lattice parameter was close to the bulk BTO crystal value. The oxygen pressure range between 15 and 20 mTorr is particularly interesting since it reflects the range where the crystal orientation changes from *c*-axis to *a*-axis oriented. A similar *c*→*a* reorientation of $Ba_xSr_{1-x}TiO_3$ (BST) films on MgO substrate has also been reported where a nearly cubic structure was found at a specific oxygen pressure [64, 65, 70]. The preferred orientation of sputter deposited polycrystalline BTO thin films on amorphous quartz, with changes from (100)/(001) to (110) orientation with increasing sputtering pressure has also been observed [59].

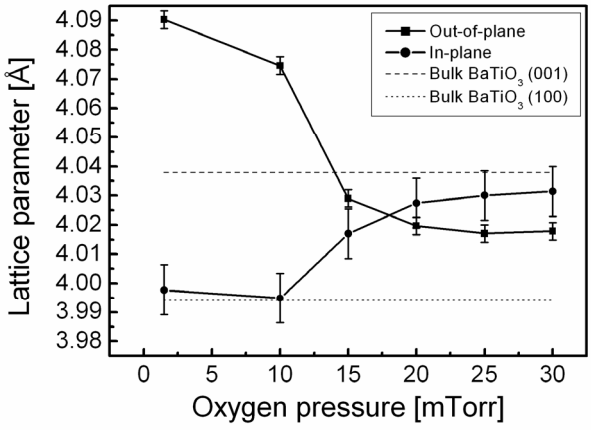

Figure 16. Out-of-plane and in-plane lattice parameters of $BaTiO_3$ thin films on MgO(001) substrates as a function of oxygen pressure during deposition. Dashed lines present the values of a- and c-lattice parameters of bulk $BaTiO_3$ at room temperature [Paper II].

The identity of the crystal phase in coherent hetero-epitaxial ferroelectric films has recently attracted much theoretical interest. Although some controversy remains with respect to the nature of the detailed temperature dependent strain-phase diagram, agreement exists with general behavior illustrated in Figure 17.

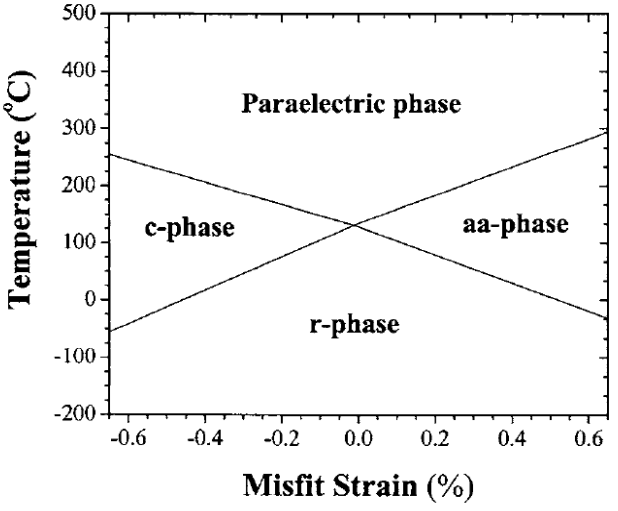

Figure 17. Theoretically obtained diagram illustrating the temperature depended phases in coherent epitaxial $BaTiO_3$ thin film on a substrate inducing a biaxial stress [56].

The substrate induced compressive biaxial stress favors the tetragonal *c*-phase with polarization vector along the <0,0,±1> direction (see for example Ref. [56]). Near the strain free region, the ferroelectric *r*-phase is monoclinic and the polarization vector points to the <n,n,m> direction. Under tensile biaxial stress, the coherent epitaxial film is in the *aa*-phase (orthorhombic) with polarization vector along the <±1,±1,0> direction. High temperature phases are non-polar paraelectric *p*-phases.

The films deposited at oxygen pressures >15 mTorr were not epitaxial, though highly oriented. Therefore, it is assumed that the substrate influence was partly relaxed due to the polycrystalline structure. In XRD off-axis measurements of the *a*-oriented films, i.e., the elongated unit cell axis is along the surface, reflections from (202) and (220) planes were undistinguishable. A similar lack of tetragonal peak splitting is reported for the epitaxial a-axis oriented BTO films on MgO(001) substrate [54]. This was attributed to a slightly different orthorhombic phase in the film from the orthorhombic phase in the bulk. In the film, the pseudocubic phase has a square in-plane lattice due to substrate constraint, while in the bulk, the unit cell is elongated along the face diagonal direction [54]. In this work, the lack of observable tetragonal splitting could also

be due to strain relaxation, so the actual phases can not be determined conclusively. However, if coherent epitaxy is maintained without defects in crystal, then the crystal phases would follow the *c*→*r*→*aa* chain along with increasing oxygen working pressure during the deposition. Potentially, 1.5 and 10 mTorr samples have a *c*-phase structure, while the 15 mTorr sample is closer to the *aa*-phase structure possessing either the *c*- or *r*-phase structure. Further pursuit of the phase evolution is not clear due to breakdown of epitaxy, but the tendency for *a*-axis orientation is observed with increasing oxygen pressure.

Figure 18 shows an AFM surface images of the samples deposited at different oxygen pressures. At low oxygen pressure, the surface is smooth with a RMS surface roughness value of unit cell order [Paper II]. The 10 mTorr oxygen pressure produced a film having a generally smooth surface with a bimodal type morphology. As the pressure was further increased, the RMS surface roughness value increased sharply when the oxygen pressure exceeded 15 mTorr but then plateaued at about 25 nm at high deposition pressures. These measurements together with XRD measurements indicate a change in the film growth mechanism from epitaxial towards polycrystalline.

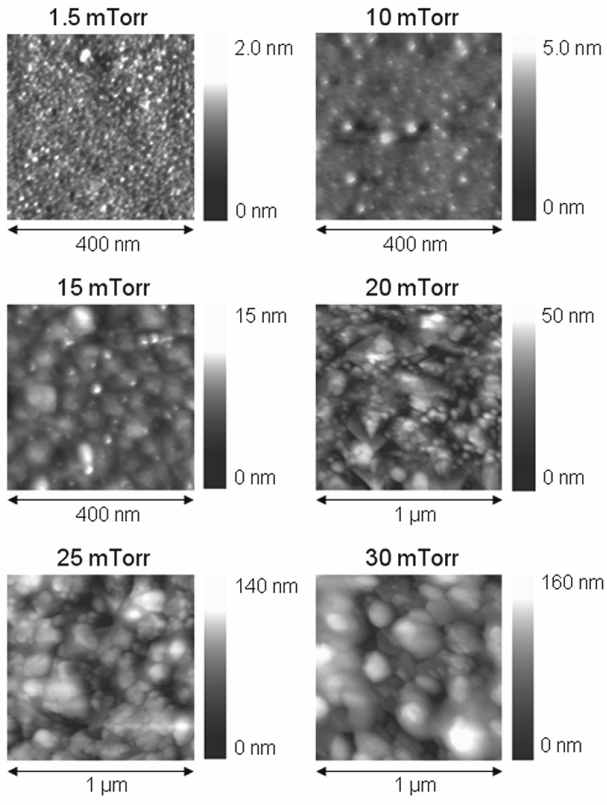

Figure 18. AFM-imaged surface morphologies of the $BaTiO_3$ thin films deposited at oxygen pressures of 1.5, 10, 15, 20, 25 and 30 mTorr, respectively [Paper II].

5.2.2 Dielectric properties

Figure 19(a) shows the normalized tunability of the relative permittivity at 1 MHz as a function of electric field for the produced $BaTiO_3$ films. During measurements, electric fields up to 3.4 V/µm were applied with no observation of the saturation of tuning. The 1.5 mTorr sample had a tunability of 5% at maximum field with a slight hysteresis behavior. The highest tunability of 9% was measured for the 10 mTorr sample. A tunability of 6% was observed for the 15 mTorr sample which exhibited a unique tunability curve characterized by the most open hysteresis loops, and a clear increase in permittivity at small electric fields. This may be explained by domain re-orientation due to the external

applied field. The slope at high fields was similar to that exhibited by the 10 mTorr sample. The hysteresis loops of the *a*-axis oriented films (20, 25 and 30 mTorr) had nearly identical tuning curves with a field insensitive region at low fields and ~5% tunability at maximum applied field with some hysteresis.

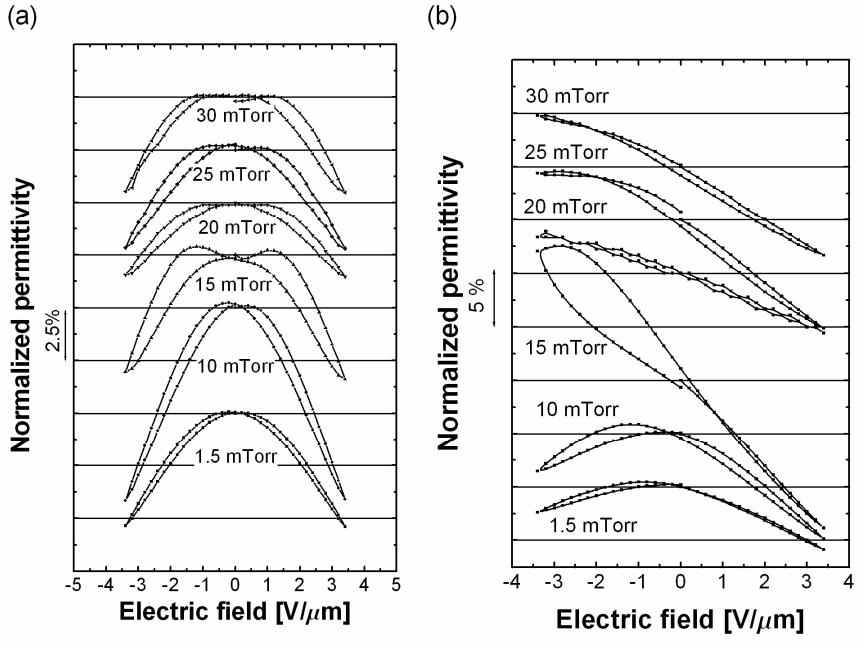

Figure 19. Normalized relative permittivity at 1 MHz as a function of bias field measured in $BaTiO_3$ films deposited at different oxygen pressures (a) before and (b) after a poling treatment [Paper II].

Figure 19(b) shows the same permittivity tuning curves after a poling treatment of these samples. In this treatment the samples were heated up to 300 °C with a DC electric field of 8 V/μm applied across the IDE finger pairs during the cooling step. As a result, the symmetric tuning curves before poling became asymmetric and generally the tunability increased. Samples deposited at 1.5 and 10 mTorr pressures exhibited <5% and 10% tunability opposite to and along the poling electric field directions respectively. The 15 mTorr sample had about 15% tunability in both directions. Along the poling direction, the hysteresis loop opening was very narrow, but the loop opened considerably in the opposite

direction. The samples deposited at 20, 25 and 30 mTorr showed also asymmetric tuning behavior after poling. The tuning curves along the poling field were almost linear with a slight hysteresis. These measurements support the observations of the polarization reorientation suggested by the XRD measurements. Generally, the *c*-oriented films were only slightly polarized after poling and the tuning curves for *a*-oriented films became nearly linear as a result of the poling treatment. The strong effect of poling on the 15 mTorr sample supports the assumption that it also has a polarization component along the surface, i.e. it can potentially be in the *r*-phase, which is also supported by the reduced tetragonality according to XRD measurements.

5.2.3 Optical properties

Figure 20(a) shows the in-plane and out-of-plane refractive indices at 633 nm. In samples deposited at 1.5, 10 and 15 mTorr oxygen pressures, the in-plane refractive index was ~2.34 while the out-of-plane value increased slightly with increasing oxygen pressure from 2.30 to 2.33. As the oxygen pressure exceeded 15 mTorr, the refractive indices decreased significantly, down to about 2.11–2.15. This is attributed to the breakdown of epitaxy as suggested by the XRD measurements and related to observations on the influence of grain size distribution on the refractive index in polycrystalline films. Figure 20(b) shows the birefringence (defined as the difference in refractive indices between the in-plane and out-of-plane values) and lattice distortion from the cubic phase (defined as 1 – [in-plane lattice parameter]/[out-of-plane lattice parameter]) as a function of oxygen pressure during film growth. The films deposited at 1.5 and 10 mTorr were strongly c-axis oriented with a high degree of birefringence. Increasing oxygen pressure decreased the tetragonal crystal distortion correlating well with reduction in birefringence. It is interesting to note the region between 15 and 20 mTorr where both the crystal distortion and birefringence change their sign as a consequence of the c→a axis crystal reorientation.

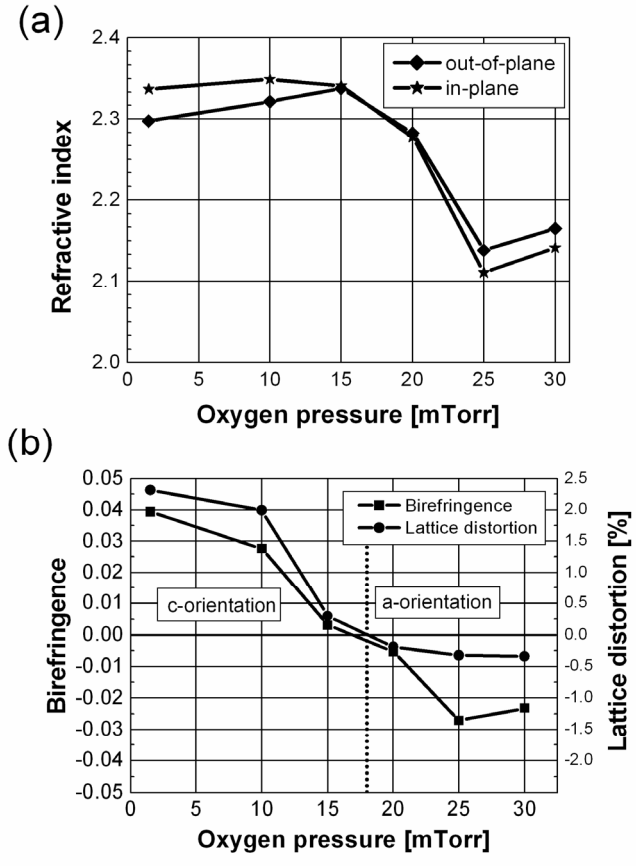

Figure 20. (a) In-plane and out-of-plane refractive indices at 633 nm wavelength in $BaTiO_3$ films deposited at different oxygen pressures. (b) Optical birefringence and lattice distortion from cubic structure determined from x-ray diffraction measurements in $BaTiO_3$ films as a function of oxygen pressure during film deposition [Paper III].

Due to the observed crystal reorientation between 10 and 20 mTorr oxygen pressure, Mach-Zehnder waveguide modulators were fabricated with samples deposited at 10, 15 and 20 mTorr oxygen partial pressures yielding BTO films with both *c*- and *a*-axis orientations, respectively. A localized intensity peak was observed at the output facet of devices fabricated with samples deposited at 10 and 15 mTorr oxygen pressures. The output intensity of the 20 mTorr sample was unlocalized, presumably due to scattering from the relatively rougher surface or from the grain boundaries in polycrystalline media. The intensities at

the Mach-Zehnder interferometer output on 10 and 15 mTorr BTO films as a function of applied electric field are plotted in Figure 21(a). The intensity curves are nonperiodic, as a function of electric field, which is a characteristic feature in the case of BTO films due to the influence of the Pockels coefficient r_{42} together with the domain poling effect as described in Section 2.2.

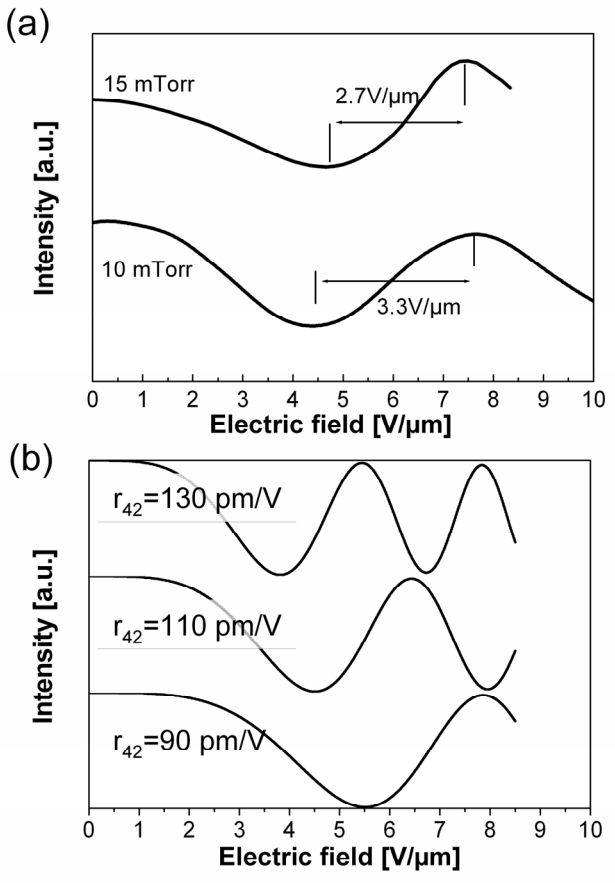

Figure 21. (a) Measured optical intensity at Mach-Zehnder waveguide modulator output facet as a function of applied electric field [Paper III]. (b) Calculated intensity modulation in a device based on the $BaTiO_3$ bulk single crystal with different r_{42} values.

The electric field (V_π/g) needed to induce peak to valley intensity modulation at high electric fields was 3.3 V/μm and 2.7 V/μm for 10 mTorr and 15 mTorr BTO film devices, respectively. In the tested structures, the overlap factor was

about 0.69 for the 10 mTorr BTO sample and 0.74 for the 15 mTorr sample. The refractive index n of the samples was approximately 2.24 at this wavelength. By substituting the appropriate terms into Expression (36), an effective electro-optic coefficient of 20 and 23 pm/V was obtained for the 10 and 15 mTorr BTO films, respectively.

Figure 21(b) shows the calculated intensity modulation as a function of an electric field obtained by using the assumption that the applied electric field is perpendicular to the polarization vector as shown Figure 7(b). The in-plane index value of 2.24 was used as n_o and n_e=2.22, which were measured values at 1550 nm for the film deposited at oxygen pressure of 10 mTorr. In calculations, the overlap factor Γ was taken into account by multiplying the phase shift by the value of 0.69. By using r_{42} value of about 110 pm/V the calculations approximate the modulation in Figure 21(a) at low electric fields. Instead at higher fields, measured periodicity of the modulation does not decrease as fast as suggested by the calculations. This indicates that though the periodicity decreases with increasing electric field, the shift in refractive index is smaller than the second-order response as assumed in calculations. This can possibly be due to substrate induced clamping preventing the rotation of the polarization.

The influence of domain structure and stress effects in BTO films has been shown to be a very significant factor in the performance of microelectronics and microphotonics devices. Substrate stabilized *c*-orientation is preferred in memory elements, where the film is sandwiched between electrodes. In electro-optic devices based on films containing *a*-oriented domains are desired enabling reduced driving voltages for the intensity modulation [60]. The reported effective electro-optic response values in BTO films consisting of partly in-plane (*a*-oriented) domains vary between 38 [71] and 360 pm/V [97].

5.3 Superlattices

5.3.1 Influence of stacking periodicity on lattice strain

Figure 22 shows a low angle region of the XRD θ-2θ diffraction patterns of five BTO-STO superlattice structures. The formation of periodic satellite peaks due

to the superlattice structure is shown in patterns from samples with short stacking periodicity in Figure 22(a). From the patterns it was possible to calculate the periodicity of the BTO-STO superlattices by the simulation of the XRD patterns shown below the measured plots in Figure 22(a). The periodicity values of 27, 49 and 105 Å were obtained with the out-of-plane lattice parameters of 4.20–4.22 Å for BTO and 3.91 Å for STO. In terms of super cells consisting of BTO and STO unit cells this would lead to the stacking periodicities of $[BTO]_{3\text{-}4}$-$[STO]_{3\text{-}4}$, $[BTO]_6$-$[STO]_6$ and $[BTO]_{13}$-$[STO]_{13}$ for the films with 27, 49 and 105 Å periodicities, respectively. This indicates the mixing of 3 and 4 unit cell stacking structures in the supercell of the shortest periodicity. The mixing was also suggested by the broadening of the measured –1 satellite reflection over the two simulated satellite reflections of the $[BTO]_3$-$[STO]_3$ and $[BTO]_4$-$[STO]_4$ structures. The *c*-lattice parameter of BTO bulk is 4.038 Å, which implies a highly strained lattice in these superlattices [25]. On the contrary, the STO lattice parameter was relatively close to the bulk value of 3.905 Å [77].

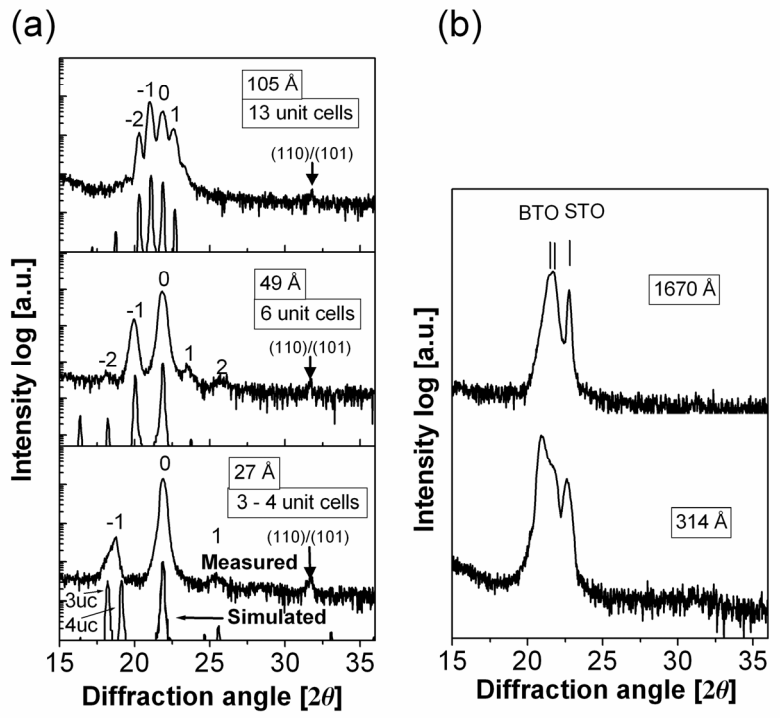

Figure 22. Measured and simulated x-ray diffraction θ-2θ patterns of the BTO-STO thin film stacks with varying stacking periodicity. (a) Measured and simulated patterns of the superlattices with periodicity of 3 & 4, 6 and 13 unit cells of both BTO and STO in the supercell. The numbers above the peaks represent the multiples of the superlattice satellite reflections. In the lowest simulation pattern, –1 satellite reflection is shown for two supercells having 3 and 4 unit cells of both BTO and STO, respectively. (b) The measured patterns of the superlattices with periodicity of 314 and 1670 Å. [Paper IV]

When the layer thickness increased, the satellite peaks were no longer observed. Instead, only the characteristic BTO and STO reflections were observed, and the periodicity was estimated by comparing the number of deposited layers with the measured total film thickness resulting in the periodicities of 314 and 1670 Å. Calculated lattice parameters in the short periodicity films were also supported by the measurement results of the films with 314 and 1670 Å periodicities. In these patterns BTO peaks were broad, indicating a strong relaxation of the out-of-plane lattice parameter. In the film with 314 Å periodicity the BTO (001) reflection shows a double peak form in Figure 22(b). This is attributed to the

relaxation of strained crystal from the lattice parameter of 4.21 Å to 4.08 Å supporting the results of highly shifted BTO out-of-plane lattice parameter in superlattices of short stacking periodicity due to interface induced stress. Similar strain relaxation was also observed in BTO-STO stack of 1670 Å periodicity. In this structure, the maximum XRD peak intensity corresponds to the lattice parameter of about 4.08 Å implying that most of the BTO lattice volume is partly relaxed. Similar type behavior of a highly strained BTO out-of-plane lattice parameter, and of a more stable STO parameter, were also observed in a previous study [73]. In this work, the high strain could also partly originate from the MgO substrate with the large temperature expansion coefficient that can put the stack in compressive stress favoring *c*-axis orientation as described in Section 3.2 [68].

The evolution of the epitaxy breakdown in stacks with thin layers is also worth noting. In the films of long periodicity (314 Å and 1670 Å), no other than (001)-based reflections were observed, while in films of short periodicity the intensity of (110)/(101) peaks increased with decreasing stacking periodicity. This is assumed to be related to the number of BTO-STO interfaces, which increases with decreasing layer thickness.

5.3.2 Optical properties

Figure 23(a) shows the out-of-plane and in-plane refractive indices at 633 nm wavelength as a function of stacking periodicity. In superlattices of short periodicity, the in-plane index is about 2.33 and out-of-plane index about 2.30. Their difference, i.e. birefringence, is plotted in Figure 23(b). It shows a slightly decreasing trend with increasing periodicity and a steeper decrease between 314 and 1670 Å stacking periodicity. This can be explained by the results of XRD measurements. The measured refractive index is an average value across the film. In 1670 Å periodicity film, most of the BTO volume was at least partly relaxed, resulting in a decrease in ion distances and thereby in an increase in out-of-plane refractive index.

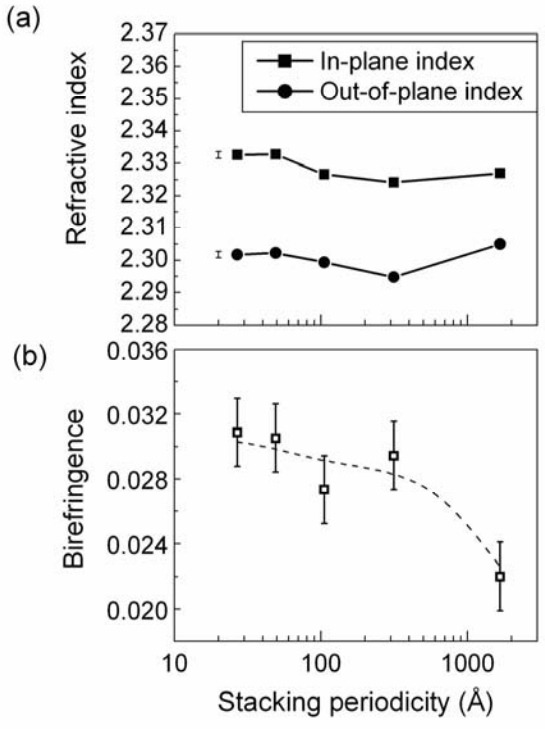

Figure 23. (a) In-plane and out-of-plane refractive indices of BTO-STO superlattices at 633 nm wavelength as a function of stacking periodicity and (b) corresponding birefringence behavior. The dashed line represents the trend line of the birefringence with increasing stacking periodicity [Paper IV].

Figure 24(a) shows the electro-optic response induced in-plane birefringence shift $\delta\Delta n$ as a function of applied electric field. The curves are plotted with the offset value of $5*10^{-5}$ for the purposes of clarity.

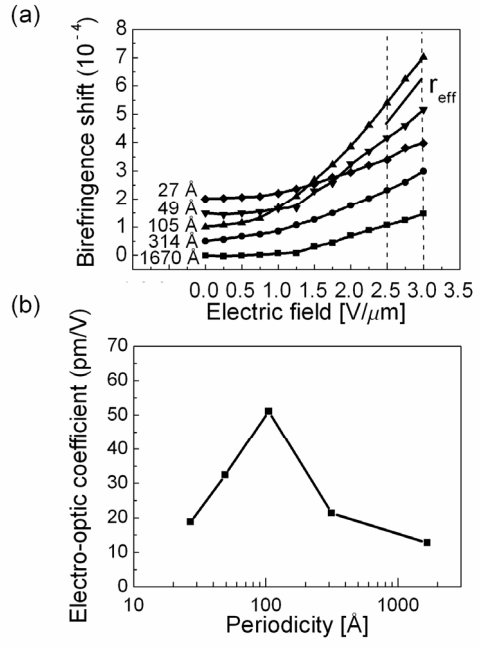

Figure 24. (a) Birefringence shift $\delta\Delta n$ of $BaTiO_3$–$SrTiO_3$ superlattices at 633 nm as a function of electric field. The dashed lines represent the region used to extract the effective linear electro-optic coefficients that are plotted as a function of stacking periodicity in (b) [Paper IV].

The shift is non-linear with a rather plateau region at low fields followed by a steeper increase. The measurements were carried out with an electric field sweep between –3 to 3 V/µm, but only the positive side is shown in Figure 24(a), since the curves were centrosymmetric. The commonly used first order effective term in Expression (3) was used to compare the strength of the electro-optic response obtained by using the linearized part between 2.5 and 3 V/µm (region between the dashed lines in Figure 24(a). Calculated *r* values as a function of stacking periodicity are plotted in Figure 22(b). As the stacking periodicity decreased from 1064 Å to 106 Å the effective electro-optic response was increased from 12 up to 51 pm/V. After reaching a maximum point, the *r* value decreased again with the decreasing periodicity.

The mechanism present in this behavior of the electro-optical response is not well understood. It can be related to observations of the permittivity and its

nonlinearity reaching maximum value at a certain stacking periodicity. Some reported superlattice stacking structures that exhibited maximum permittivity values in these superlattices are collected in Table 1. In Refs. [98, 99 and 100], the permittivity decreases with both increasing and decreasing stacking periodicity around the maximum point. Also rather monotonically increasing permittivity with decreasing stacking periodicity have been reported in experimental works [73, 75, 82, 101, 102]. In Ref. [82] an electro-optic response was also studied as a function of the stacking periodicity, and it was found to increase more than an order in magnitude when permittivity increased by 50%.

Table 1. Reported stacking structures of different superlattices having the maximum permittivity value in each studied group of superlattices (see text).

Material	Stacking periodicity for max permittivity	Measure-ment direction	Epitaxial/ Poly-crystalline	Ref.
$BaTiO_3$-$SrTiO_3$	2 × 10 unit cells	In-plane	Epitaxial	[98]
$BaTiO_3$-$BaZrO_3$	2 × 10 unit cells	In-plane	Epitaxial	[99]
$BaTiO_3$-$SrTiO_3$	2 × 20 nm	Out-of-plane	Polycrystalline	[100]
$BaTiO_3$-$SrTiO_3$	2 × (3–5) unit cells	Out-of-plane	-	[75]
$BaTiO_3$-$SrTiO_3$	2 × (2–4) unit cells	Out-of-plane	Epitaxial	[73]
$BaTiO_3$-$SrTiO_3$	2 × 1 nm	Out-of-plane	Epitaxial	[101]
$Ba_{0.8}Sr_{0.2}TiO_3$-$Ba_{0.4}Sr_{0.6}TiO_3$	4 unit cells	Out-of-plane	Epitaxial	[102]
$Pb(Mg_{1/3}Nb_{2/3})O_3$ $PbTiO_3$	10 nm	Out-of-plane	Epitaxial	[82]

Whether BTO or STO layer gives a major rise in the enhancement of the electro-optic response in BTO-STO superlattices is not known. Permittivity in STO is not tunable at room temperature in bulk, but it has been shown that in a thin film after manipulation of the stress state its tunability can increase significantly even in a single layer STO film [103].

Though the trend line of the electro-optic response as a function of stacking periodicity in Figure 24(b) resembles the observations of reported permittivity along the in-plane direction, the response can be influenced by the internal dipole structure. In this work, the electric field inducing the electro-optic response was along the in-plane direction.

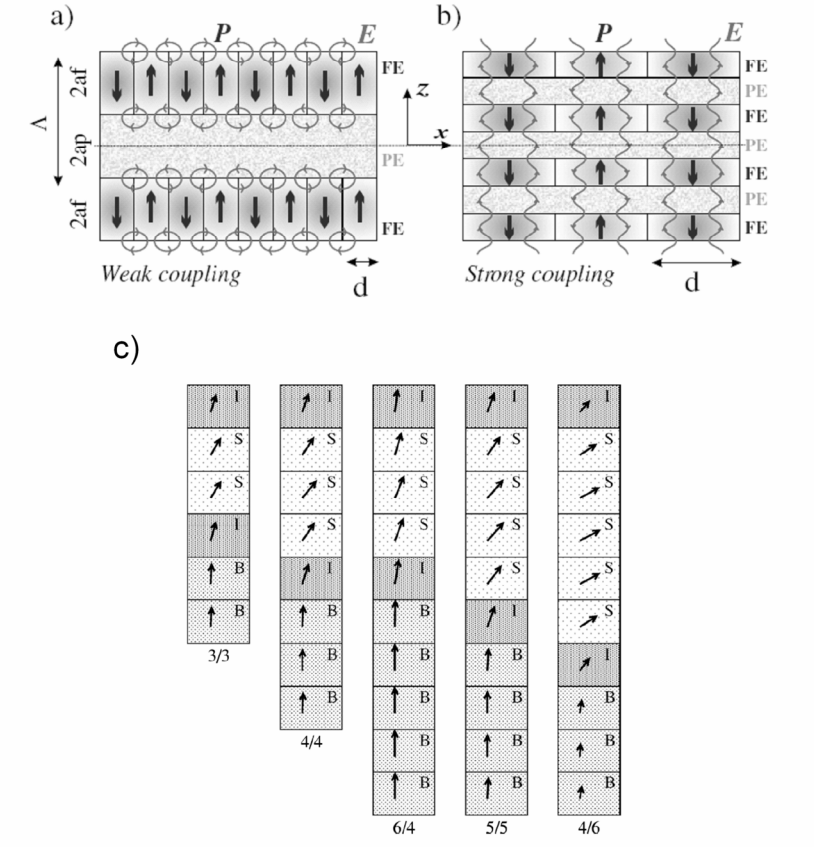

Figure 25. (a) Weak and (b) strong coupling between ferreoelectric layers in ferroelectric (FE) – paraelectric (PE) superlattice [79]. (c) Polarization orientation in BTO-STO multilayers. SrTiO3, BaTiO3 and interface cells are labeled as S, B and I, respectively [104].

Both computational [79, 104, 105] and experimental [81] works suggest that the internal dipole structure is sensitive to the stacking periodicity. For long stacking periodicity each ferroelectric layer has an independent domain structure with depolarization fields, and layers are said to be weakly coupled, which is

illustrated in Figure 25(a). Below a critical layer thickness, the layers are coupled via electric field arising from ferroelectric layers, and then the superlattice structure behaves as an uniform material [79] as illustrated in Figure 25(b). First-principle computational studies predict that the BTO-STO superlattices of short periodicity behave as a homogenous material with a temperature dependent phase diagram resembling that of pure BTO film shown in Figure 17 [105]. Instead, in the superlattices of longer periodicity, the polarization reorientation from out-of-plane to in-plane occurs in STO layer with increasing stacking periodicity [104]. This is explained by the larger lattice parameter of BTO than that of STO, resulting in a tensile stress in the STO layer and a more compressive stress in the BTO layer. Figure 25(c) shows calculated polarization distributions in BTO-STO superlattices illustrating the possibility of different polarization distributions in BTO and STO layers.

In addition, decreasing compressive stress originating from the MgO substrate results in a reorientation of the polarization first in STO. Further increase of the tensile strain leads to the disappearance of out-of-plane polarization also in the BTO layer, in favor of the in-plane *aa*-phase. Computational studies also indicate that both the out-of-plane and in-plane permittivity can increase significantly along with the strain shift maximum value near the polarization reorientation point [105, 106]. The stress state relaxation observed in this work with increasing stacking periodicity can possibly also influence the increase of the tuning properties. Potentially, a certain stacking structure can thereby lead to an optimal response for a specific electric field direction. It is also possible that the grain boundaries, due to the breakdown of epitaxy, can reduce the external electric field penetration inside the superlattice columns.

The suitability of BTO-STO superlattices for the waveguide applications were evaluated by manufacturing and characterizing waveguide Mach-Zehnder devices [V]. According to the XRD measurements, each layer in the superlattice consisted of 11 unit cells. The cross section of the active arm of the intensity modulator and some measurement results with it are shown in Figure 26. The localized near field intensity distribution at the output facet of the device shown in Figure 26(b) confirmed the proper waveguiding operation and possibility to use ferroelectric-paraelectric superlattices in planar optical applications. An applied electric field across the active arm of the Mach-Zehnder device caused an intensity modulation shown in Figure 26(c). An effective electro-optic

coefficient of 73 pm/V was obtained for the BTO-STO superlattice film by substituting the appropriate terms into Equation (19). Utilizing the same Mach-Zehnder structure and processing conditions, but substituting the BTO-STO superlattice with a single layer BTO film, a r_{eff} value of only about 23 pm/V was obtained as explained in Section 5.2.3.

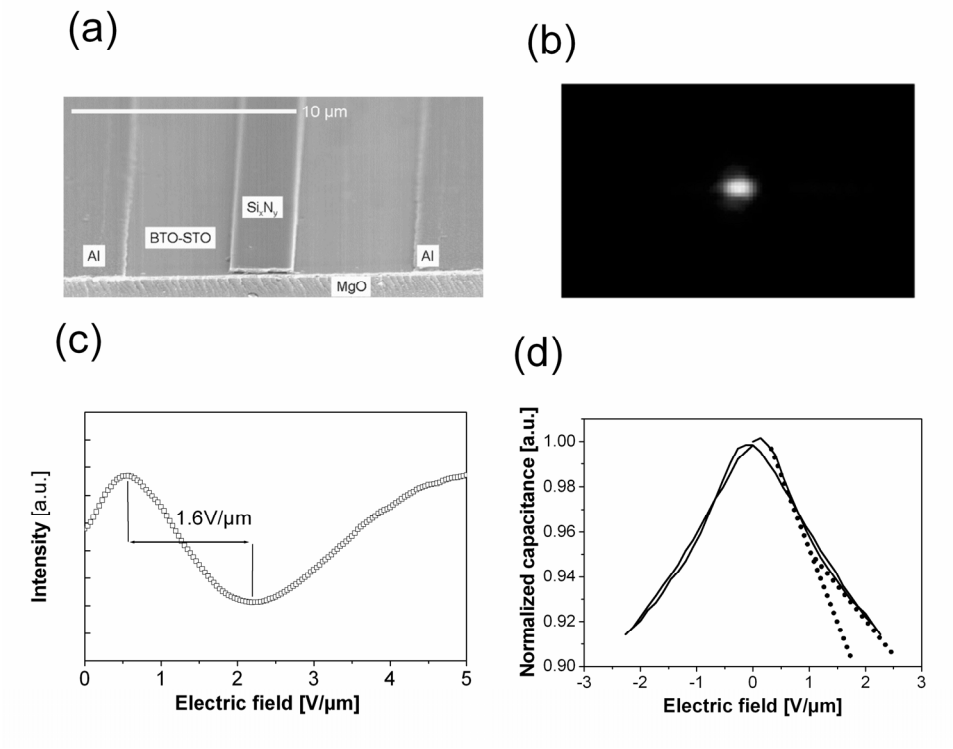

Figure 26. A demonstration of ferroelectric-paraelectric superlattice waveguide device. (a) Cross section SEM-image of the device and (b) an intensity distribution image taken at the Mach-Zehnder waveguide output facet. (c) The intensity at the Mach-Zehnder modulator output as a function of the applied electric field and (d) the normalized capacitance of the device at 1 MHz frequency as a function of bias electric field. The dashed lines show the variation in tuning slope in different electric field regions.

The form of the intensity modulation as a function of the electric field is interesting to note. The modulation periodicity increases at high electric field values, indicating a reduction in the effective electro-optic response. Figure

26(d) shows the normalized capacitance of the device at 1 MHz frequency as a function of the electric field. A trend for the saturation was observed at high field values due to reduced capacitance tuning behavior. At the used 1 MHz measurement frequency, ions can follow the field. As the ion displacement induces a refractive index shift, it is believed that this indicates the correlation between the low frequency (1 MHz) and optical frequency tunability, i.e., the shift in refractive index due to displaced ions. In the case of single layer BTO films no sign of saturation in capacitance or optical modulation was observed with used electric fields.

6. Conclusions and outlook

The motivation for this work was to gain improved understanding of the micro- and nanostructure influence on the optical properties of active ferroelectric thin films with the view towards the manufacture of functional devices for photonics. Three micro- and nanostructure effects were studied in this thesis: i) grain size effects, ii) crystal orientation related properties in both epitaxial and polycrystalline films and iii) some influences of superlattice periodicity. Different micro- and nanostructures were obtained by tuning the processing conditions in the fabrication of thin films by pulsed laser deposition (PLD).

Different grain size distributions in PNZT thin films were produced by pulsed laser deposition on MgO(001) substrates at room temperature and post-annealing at temperatures between 700 ºC – 900 °C. Both the refractive index and electro-optic coefficient of the films were found to increase with increasing mean grain size. The value of the electro-optic coefficient increased from 0.37×10^{-18} m^2/V^2 up to $\sim2\times10^{-18}$ m^2/V^2 and the value of the refractive index increased from 2.28 to 2.46 with increasing mean grain size from 91 Å to 213 Å, respectively.

The crystal structure of BTO thin films grown on MgO(001) substrates at 700 °C by PLD was found to be strongly influenced by the oxygen partial pressure used during growth. According to the x-ray diffraction measurements, low oxygen pressures produced *c*-axis oriented films and roughness only of the order of a unit cell length. With increasing oxygen pressure, the out-of-plane lattice parameter decreased, while the in-plane value increased resulting in reorientation to the *a*-axis orientation with a concomitant increase in polycrystallinity and surface roughness up to RMS values over 20 nm, which are too high, e.g., for optical devices.

This thesis includes the first electrical poling and optical birefringence studies on the BTO lattice strains and on the direction of the polarization as a function of background oxygen pressure during the pulsed laser deposition. In poling experiments, the non-linear permittivity was characterized before and after the poling treatment at elevated temperature. Poling altered only a slightly the form of the tuning curves in *c*-oriented samples. Instead, in *a*-oriented samples the tuning curves became almost linear as a result of the situation where the main electric field component was applied along the polarization direction, because of

the IDE electrode configuration. The influence of the crystal reorientation resulted in the change of the sign of the optical birefringence correlating well with XRD and electrical measurements. The surface roughness of the *c*-oriented films was sufficiently low making possible the fabrication of Mach-Zehnder waveguide modulators. The measured operation of the devices was compared with the calculated operation of similar devices based on the bulk $BaTiO_3$. The calculations approximate the modulation at low electric fields. Instead at higher fields, measured periodicity of the modulation in thin film device does not decrease as fast as suggested by the calculations. Effective electro-optic responses of ~21 pm/V were obtained for BTO films.

This thesis includes also the first studies on the directional dependent refractive index, and the electro-optic response in BTO-STO superlattices with varying stacking periodicity. These superlattice thin films with periodicity between 27 and 1670 Å were grown on MgO(001) substrates. XRD measurements suggested a highly strained out-of-plane lattice constant of 4.20–4.22 Å in BTO layers due to interface induced stress. On the contrary, the value of the STO lattice constant was found to be relatively close to the bulk value. The stress in BTO layers was relaxed as the layer thickness increased. The influence of strain relaxation in the BTO layer was also found in optical birefringence measurements as the birefringence decreased together with crystal strain relaxation. The electro-optic response was found to increase with decreasing stacking periodicity in superlattice stacks of BTO-STO and obtained a maximum value of 51 pm/V in a superlattice stack of 105 Å periodicity. A further reduction in stacking periodicity resulted in a decrease in effective electro-optic coefficient. The suitability of these superlattices for in planar waveguide devices was evaluated by fabricating Mach-Zehnder devices as the first published device application of these superlattices [Paper V], and their operation was confirmed by observing proper waveguiding and intensity modulation due to the electro-optic effect. Effective electro-optic coefficient value of 73 pm/V was obtained for the device fabricated on the BTO/STO stack with 11 BTO and STO unit cells in a super cell.

In this work, the processing conditions were found to be an important parameter in the tuning of the optical properties of ferroelectric thin films. Recently, substrate induced stress issues have been a notable topic in manipulating the general physical properties of these materials in thin film forms. Since, all the

films in this study were grown on MgO(001) substrates, it would be beneficial to study how the manipulation of the properties by the processing conditions are transferred to films with different substrate-originated stress states. Also, further computational studies are required to explain comprehensively the observations of the microstructure and superlattice effects on the dielectric and optical response.

Technologically important issues include the integration of ferroelectrics on semiconductor substrates to combine the superior electrical and light generation properties of semiconductors and the electric-field induced activity of the ferroelectrics [107, 108]. Another important research topic is the study of the high-frequency responses of the films. This would require a careful design of both optical and RF-electronics devices besides the optimized fabrication processes [18]. Pulsed laser deposition is mainly used in research purposes due to its relatively low equipment costs and versatility in depositing a wide range of materials and multilayer structures. It has, however, drawbacks limiting its use in volume production. This includes the difficulty to cover large areas of wafers uniformly and without particulates of target material [14]. If other vacuum deposition methods are therefore required for larger production volumes, the studies in this thesis to manipulate the micro- and nanostructures and consequently physical properties of the films are relevant also for other processes like MBE or sputtering.

References

[1] Hunsperger, R. G. Integrated Optics Theory and Technology. Fourth Edition. Springer, 1995. Chapter 1. ISBN 3-540-59481-7.

[2] Nishihara, H., Haruna, M. and Suhara, T. Optical Integrated Circuits. New York, NY: McGraw-Hill Publishing Company, 1985. Chapter 1. ISBN 0-07-046092-2.

[3] Papannareddy, R. Introduction to Lightwave Communication Systems. Boston, MA: Artech House, 1997. ISBN 0-89006-572-1.

[4] Saleh, B. E. A. and Teich, M. C. Fundamentals of Photonics. John Wiley & Sons, Inc., 1991. P. 240. ISBN 0-471-83965-5.

[5] Towe, E. Heterogeneous Optoelectronics Integration. Bellingham, Washington: SPIE-The International Society for Optical Engineering. Bellingham, WA: SPIE Press, 2000. Chapter 1. ISBN 0-8194-3571-6.

[6] Heikkinen, V. Tunable laser module for fibre optic communications. Thesis. VTT Publications 528. Espoo: VTT, 2004. ISBN 951-38-6375-1.

[7] Nishihara, H., Haruna, M. and Suhara, T. Optical Integrated Circuits. New York, NY: McGraw-Hill Publishing Company, 1985. Chapters 9–10. ISBN 0-07-046092-2.

[8] Nishihara, H., Haruna, M. and Suhara, T. Optical Integrated Circuits. New York, NY: McGraw-Hill Publishing Company, 1985. Chapter 10. ISBN 0-07-046092-2.

[9] Uchino, K. Ferroelectric Devices. New York, NY: Marcel Dekker, Inc., 2000. ISBN 0-8247-8133-3.

[10] Nishihara, H., Haruna, M. and Suhara, T. Optical Integrated Circuits. New York, NY: McGraw-Hill Publishing Company, 1985. Chapter 6. ISBN 0-07-046092-2.

[11] Buchal, Ch., Beckers, L., Eckau, A., Schubert, J. and Zander, W. Epitaxial $BaTiO_3$ thin films on MgO. Materials Science and Engineering B, 1998. Vol. 56, pp. 234–238.

[12] Schwarzkopf, J. and Fornari, R. Epitaxial growth of ferroelectric oxide films. Progress in Crystal Growth and Characterization of Materials, 2006. Vol. 52, pp. 159–212.

[13] Whatmore, R. W., Zhang, Q., Huang, Z. and Dorey, R. A. Ferroelectric thin and thick films for microsystems. Materials Science in Semiconductor Processing, 2003. Vol. 5, pp. 65–76.

[14] Chiresy, D. B. and Hubler, G. K. Pulsed Laser Deposition of Thin Films. New York, NY: John Wiley & Sons, 1994. ISBN 0-471-59218-8.

[15] Kreutz, E. W. and Gottman, J. PLD of perovskite coatings for optoelectronics, microelectronics, and microtechnology. Journal of the European Ceramic Society, 2004. Vol. 24, pp. 979–984.

[16] Schlom, D. G., Haeni, J. H., Lettieri, J., Theis, C. D., Tian, W., Jiang, J. C. and Pan, X. Q. Oxide nano-engineering using MBE. Materials Science and Engineering B, 2001. Vol. 87, pp. 282–291.

[17] Adachi, H. and Wasa, K. Sputtering Preparation of Ferroelectric PLZT Thin Films and Their Optical Applications. IEEE Transactions on Ultrasonics and Frequency Control, 1991. Vol. 38, pp. 645–655.

[18] Tang, P., Towner, D. J., Hamano, T., Meier, A. L. and Wessels, B. W. E. Electro-optic modulation up to 40 GHz in a barium titanate thin film waveguide modulator. Optics Express, 2004. Vol. 12, pp. 5962–5967.

[19] Nishihara, H., Haruna, M. and Suhara, T. Optical Integrated Circuits. New York, NY: McGraw-Hill Publishing Company, 1985. Chapter 8.4. ISBN 0-07-046092-2.

[20] Fork, D. K., Armani-Leplingard, F. and Kingston, J. J. Optical Losses in Ferroelectric Oxide Thin Films: Is There Light at the End of the Tunnel? Materials Research Society Symposium Proceedings, 1995. Vol. 361, pp. 155–166.

[21] Lines, M. E. and Glass. A. M. Principles and Applications of Ferroelectrics and Related Materials. Oxford: Oxford University Press, 1977. ISBN 0-19-850778.

[22] Jaffe, B., Cook, W. R. and Jaffe, H. Piezoelectric ceramics. London and New York, NY: Academic Press, 1971. ISBN 0-12-379550-8.

[23] Bhattacharya, K. and Ravichandran, G. Ferroeelctric perovskites for electromechanical actuation. Acta Materialia, 2003. Vol. 51, pp. 5941–5960.

[24] Kholkin, A., Jadidian, B. and Safari, A. Ceramics, Piezoelectric and Electrostrictive. In: Encyclopedia of Smart Materials, Edited by Schwartz, M. John Wiley & Sons, 2002. ISBN 978-0-471-17780-7.

[25] Powder Diffraction File, Card No 00-005-0626. Newton Square, PA: International Centre for Diffraction Data.

[26] Hu, T. BST-Based Low Temperature Co-Fired Ceramic (LTCC) Modules for Microwave tunable Components. Thesis. Oulu: University of Oulu, 2004. ISBN 951-42-7291-9.

[27] Gevorgian, S. S. and Kollberg, E. L. Do We Really Need Ferroelectrics in Paralectric Phase Only in Electrically Controlled Microwave Devices? IEEE Transactions on Microwave Theory and Techniques, 2001. Vol. 49, pp. 2117–2124.

[28] Abe, K. and Komatsu, S. Ferroelectric properties in epitaxially grown $Ba_xSr_{1-x}TiO_3$ thin films. Journal of Applied Physics, 1995. Vol. 77, pp. 6461–6465.

[29] Gevorgian, S., Petrov, P. K., Ivanov, Z. and Wikborg, E. Tailoring the temperature coefficient of capacitance in ferroelectric varactors. Applied Physics Letters, 2001. Vol. 79, pp. 1861–1863.

[30] Qiu, J. H. and Jiang, Q. Film thickness dependence of electro-optic effects in epitaxial $Ba_{0.7}Sr_{0.3}TiO_3$ thin films. Journal of Applied Physics, 2007. Vol. 102, Article 074101.

[31] Uchino, K. Relaxor Ferroelectric devices. Ferroelectrics, 1994. Vol. 151, pp. 321–330.

[32] Cross, L. E. Relaxor Ferroelectrics. Ferroelectrics, 1994. Vol. 151, pp. 305–320.

[33] Ramtron International Corporation. www.ramtron.com.

[34] Kingery, W. D., Bowen, H. K. and Uhlman, D. R. Introduction to Ceramics. Second edition. New York, NY: John Wiley & Sons, 1976. Chapter 18. ISBN 0-471-47860-1.

[35] Yariv, A. Optical Electronics in Modern Communications. New York, NY: Oxford University Press, 1997. Chapter 9. ISBN 0-19-510626-1.

[36] Blomqvist, M. Electro-Optical $Na_{0.5}K_{0.5}NbO_3$ Films. Thesis. Stockholm: Kungliga Tekniska Högskolan, 2005.

[37] Meng, X. Y., Wang, Z. Z. and Chen, C. Mechanism of the electro-optic effect in $BaTiO_3$. Chemical Physics Letters, 2005. Vol. 411, pp. 357–360.

[38] Saleh, B. E. A. and Teich, M. C. Fundamentals of Photonics. John Wiley & Sons, Inc., 1991. Chapter 18. ISBN 0-471-83965-5.

[39] Kingery, W. D., Bowen, H. K. and Uhlman, D. R. Introduction to Ceramics. Second edition. New York, NY: John Wiley & Sons, 1976. Pp. 660–661. ISBN 0-471-47860-1.

[40] Zgonik, M., Bernasconi, P., Duelli, M., Schlesser, R., Günter, P., Garrett, M. H., Rytz, D., Zhu, Y. and Wu, X. Dielectric, elastic, piezoelectric, electro-optic, and elasto-optic sensors of $BaTiO_3$ crystals. Physical Review B, 1994. Vol. 50, pp. 5491–5950.

[41] Avrahami, Y. $BaTiO_3$ based materials for Piezoelectric and Electro-optic Applications. Thesis. Cambridge, MA: Massachusetts Institute of Technology, 2003.

[42] Petraru, A., Schubert, J., Schmid, M. and Buchal, Ch. Ferroelectric $BaTiO_3$ thin-film optical waveguide modulators. Applied Physics Letters, 2002. Vol. 81, pp. 1375–1377.

[43] Saleh, B. E. A. and Teich, M. C. Fundamentals of Photonics. John Wiley & Sons, Inc., 1991. Chapter 6. ISBN 0-471-83965-5.

[44] Chen, D.-Y. and Phillips, J. D. Analysis and Design Optimization of Electrooptic Interferometric Modulators for Microphotonics Applications. Journal of Lightwave Technology, 2006. Vol. 24, pp. 2340–2346.

[45] Saleh, B. E. A. and Teich, M. C. Fundamentals of Photonics. John Wiley & Sons, Inc., 1991. Chapter 2.5. ISBN 0-471-83965-5.

[46] Chen, D.-Y. and Phillips, J. D. Hysteric electro-optic response in ferroelectrics thin films. Proceedings of SPIE, 2005. Vol. 5867, Article 58670B.

[47] Berger, S. Size effect in thin ferroelectric films. Trends in Vacuum Science and Technology, 2004. Vol. 6, pp. 1–14.

[48] Hoshina, T., Kakemoto, H., Tsurumi, T., Wada, S. and Yashima, M. Size and temperature induced phase transition behaviors of barium titanate nanoparticles. Journal of Applied Physics, 2006. Vol. 99, Article 054311.

[49] Lappalainen, J. Laser-Ablation Deposition and Characterization of Polycrystalline Nd-Modified $Pb(Zr,Ti)O_3$ Thin Films. Thesis. Oulu: University of Oulu, 1999. ISBN 951-42-5430-9.

[50] Choi, K. J., Biegalski, M., Li, Y. L., Sharan, A., Schubert, J., Uecker, R., Reiche, P., Chen, Y. B., Pan, X. Q., Gopalan, V., Chen, L.-Q., Schlom, D. G. and Eom, C. B. Enhancement of Ferroelectricity in Strained $BaTiO_3$ Thin Films. Science, 2004. Vol. 306, pp. 1005–1009.

[51] Bai, F., Zheng, H., Cao, H., Cross, L. E., Ramesh, R., Li, J. and Viehland, D. Epitaxially induced high temperature (>900 K) cubic-tetragonal structural phase transition in $BaTiO_3$ thin films. Applied Physics Letters, 2004. Vol. 85, pp. 4109–4111.

[52] Li, Y. L. and Chen, L. Q. Temperature-strain phase diagram for $BaTiO_3$ thin films. Applied Physics Letters, 2006. Vol. 88, Article 072905.

[53] Yoneda, Y., Okabe, T., Sakaue, K., Terauchi, H., Kasatani, H. and Degushi, D. Structural characterization of $BaTiO_3$ thin films grown by molecular beam epitaxy. Journal of Applied Physics, 1998. Vol. 83, pp. 2458–2461.

[54] He, F. and Wells, B. O. Lattice strain in epitaxial $BaTiO_3$ thin films. Applied Physics Letters, 2006. Vol. 88, Article 152908.

[55] Lai, B.-K., Kornev, I. A., Bellaiche, L. and Salamo, G. J. Phase diagrams of epitaxial $BaTiO_3$ ultrathin films from first principles. Applied Physics Letters, 2005. Vol. 86, Article 132904.

[56] Misirlioglu, I. B., Alpay, S. P., He, F. and Wells, B. O. Stress induced monoclinic phase in epitaxial $BaTiO_3$ on MgO. Journal of Applied Physics, 2006. Vol. 99, Article 104103.

[57] Diéguez, O., Tinte, S., Antons, A., Bungaro, C., Neaton, J. B., Rabe, K. M. and Vanderbilt, D. *Ab initio* study of the phase diagram of epitaxial $BaTiO_3$. Physical Review B, 2004. Vol. 69, Article 212101.

[58] Pertsev, N. A., Zembilgotov, A. G. and Tagantsev, A. K. Effect of Mechanical Boundary Conditioins on Phase Diagrams of Epitaxial Ferroelectric Thin Films. Physical Review Letters, 1998. Vol. 80, pp. 1988–1991.

[59] Lee, N.-L., Sekine, T., Ito, Y. and Uchino, K. Deposition Profile of RF-Magnetron-Sputtered $BaTiO_3$ Thin Films. Japanese Journal of Applied Physics, 1994. Vol. 33, pp. 1484–1488.

[60] Mi, S. B., Jia, C. L., Heeg, T., Trithaveesak, O., Schubert, J. and Urban, K. Heterostructures of $BaTiO_3$ bilayer films on $SrTiO_3$ (001) under different oxygen pressures. Journal of Crystal Growth, 2005. Vol. 283, pp. 425–429.

[61] Guo, H. Z., Chen, Z. H., Cheng, B. L., Lu, H. B., Liu, L. F. and Zhou, Y. L. Structure dynamics of strongly reduced epitaxial $BaTiO_{3-x}$ studied by Raman scattering. Journal of the European Ceramics Society, 2005. Vol. 25, pp. 2347–2351.

[62] Zhang, J., Cui, D., Zhou, Y., Li, L., Chen, Z., Szabadi, M. and Hess, P. Effect of oxygen pressure on the orientation, lattice parameters, and surface morphology of laser ablated $BaTiO_3$ thin films. Thin Solid Films, 1996. Vol. 287, pp. 101–103.

[63] Tarsa, E. J., Hachfeld, E. H., Quinlan, F. T., Speck, J. S. and Eddy, M. Growth-related stress and surface morphology in homoepitaxial $SrTiO_3$ films. Applied Physics Letters, 1996. Vol. 68, pp. 490–492.

[64] Kim, W. J., Chang, W., Qadri, S. B., Pond, J. M., Kirchoefer, S. W., Chirsey, D. B. and Horwitz, J. S. Microwave properties of tetragonally distorted $(Ba_{0.5}Sr_{0.5})TiO_3$ thin films. Applied Physics Letters, 2000. Vol. 76, pp. 1185–1187.

[65] Bellotti, J. A., Chang, W., Qadri, S. B., Kirchoefer, S. W. and Pond, J. M. Directionally dependent ferroelectric phase transition order of anisotropic epitaxial $Ba_xSr_{1-x}TiO_3$ thin films. Applied Physics Letters, 2006. Vol. 88, Article 012902.

[66] Trithaveesak, O., Schubert, J. and Buchal, Ch. Ferroelectric properties of epitaxial $BaTiO_3$ thin films and heterostructures on different substrates. Journal of Applied Physics, 2005. Vol. 98, Article 114101.

[67] Beckers, L., Schubert, J., Zander, W., Ziesmann, J., Eckau, A., Leinenbach, P. and Buchal, Ch. Structural and optical characterization of epitaxial waveguiding $BaTiO_3$ thin films on MgO. Journal of Applied Physics, 1998. Vol. 83, pp. 3305–3310.

[68] Srikant, V., Tarsa, E. J., Clarke, D. R. and Speck, J. S. Crystallographic orientation of epitaxial $BaTiO_3$ films: The role of thermal-expansion mismatch with the substrate. Journal of Applied Physics, 1995. Vol. 77, pp. 1517–1522.

[69] Powder Diffraction File, Card No 00-045-0946. Newton Square, PA: International Centre for Diffraction Data.

[70] Kim, W. J., Wu, H. D., Chang, W., Qadri, S. B., Pond, J. M., Kirchoefer, S. W., Chirsey, D. B. and Horwitz, J. S. Microwave dielectric properties

of strained $(Ba_{0.4}Sr_{0.6})TiO_3$ thin films. Journal of Applied Physics, 2000. Vol. 88, pp. 5448–5451.

[71] Tang, P., Towner, D. J., Meier, A. L. and Wessels, B. W. Low-Loss Electrooptic $BaTiO_3$ Thin Film Waveguide Modulator. IEEE Photonics Technology Letters, 2004. Vol. 16, pp. 1837–1839.

[72] Yuan, Z., Lin, Y., Weaver, J., Chen, X., Chen, C. L., Subramanyam, G., Jiang, J. C. and Meletis, E. I. Large dielectric tunability and microwave properties of Mn-doped $(Ba,Sr)TiO_3$ thin films. Applied Physics Letters, 2005. Vol. 87, Article 152901.

[73] Tabata, H., Tanaka, H. and Kawai, T. Formation of artificial $BaTiO_3/SrTiO_3$ superlattice using pulsed laser deposition and their dielectric properties. Applied Physics Letters, 1994. Vol. 65, pp. 1970–1972.

[74] Kim, J., Kim, Y., Kim, Y. S., Lee, J., Kim, L. and Jung, D. Large nonlinear dielectric properties of artificial $BaTiO_3/SrTiO_3$ superlattices. Applied Physics Letters, 2002. Vol. 80, pp. 3581–3583.

[75] Shimuta, T., Nakagawara, O., Makino, T., Arai, S., Tabata, H. and Kawai, T. Enhancement of remanent polarization in epitaxial $BaTiO_3/SrTiO_3$ superlattices with “asymmetric” structure. Journal of Applied Physics, 2002. Vol. 91, pp. 2290–2294.

[76] Tenne, D. A., Bruchhausen, A., Lanzillotti-Kimru, N. D., Fainstain, A., Katiyar, R. S., Cantarero, A., Soukissian, A., Vaithyanathan, V., Haeni, J. H., Tian, W., Schlom, D. G., Choi, K. J., Kim, D. M., Eom, C. B., Sun, H. P., Pan, X. Q., Li, Y. L., Chen, Q. X., Jia, Q. X., Nakhmanson, S. M., Rabe, K. M. and Xi, X. X. Probing Nanoscale Ferroelectricity by Ultraviolet Raman Spectroscopy. Science, 2006. Vol. 313, pp. 1614–1616.

[77] Powder Diffraction File, Card No 00-035-0734. Newton Square, PA: International Centre for Diffraction Data.

[78] Zhong, S., Alpay, S. P. and Mantese, J. V. High dielectric tunability in ferroelectric-paralectric bilayers and multilayer superlattices. Applied Physics Letters, 2006. Vol. 88, Article 132904.

[79] Stephanovic, V. A., Luk'yanchuck, I. A. and Karkut, M. G. Domain-Enhanced Interlayer Coupling in Ferroelectric/Paralectric Superlattice. Physical Review Letters, 2005. Vol. 94, Article 047601.

[80] Zhao, T., Chen, Z.-H., Chen, F., Shi, W. S., Lu, H.-B. and Yang, G.-Z. Enhancements of second-harmonic generation in $BaTiO_3/SrTiO_3$ superlattices. Physical Review B, 1999. Vol. 60, pp. 1697–1700.

[81] Jiang, A. Q., Scott, J. F., Lu, H. and Chen, Z. Phase transitions and polarizations in epitaxial $BaTiO_3/SrTiO_3$ superlattices studied by second-harmonic generation. Journal of Applied Physics, 2003. Vol. 93, pp. 1180–1185.

[82] Lu, Y. and Knize, R. J. Enhanced dielectric and electro-optic effects in relaxor oxide heterostructured superlattices. Journal of Physics D: Applied Physics, 2004. Vol. 37, pp. 2432–2436.

[83] Klug, H. P. and Alexander, L. E. X-ray Diffraction Procedures for Polycrytalline and Amorphous Materials. New York, NY: John Wiley & Sons Ltd, 1974. Pp. 643–665.

[84] Warren, B. E. X-ray Diffraction. Reading, MA: Addison-Wesley Publishing Company, 1969.

[85] Cullity, B. D. Elements of X-ray Diffraction. Reading, MA: Addison-Wesley Publishing Company, 1967. ISBN 0-201-01230-8.

[86] Al-Shareef, H. N., Dimos, D., Raymond, M. V., Schwartz, R. W. and Mueller, C. H. Tunability and Calculation of the Dielectric Constant of Capacitor Structures with Interdigital Electrodes. Journal of Electroceramics, 1997. Vol. 1, No. 2, pp. 145–153.

[87] Wang, D. Y., Lor, K. P., Chung, K. K., Chan, H. P., Chiang, K. S., Chan, H. L. W. and Choy, C. L. Optical rib waveguide based on epitaxial

$Ba_{0.7}Sr_{0.3}TiO_3$ thin film grown on MgO. Thin Solid Films, 2006. Vol. 510, pp. 329–333.

[88] Tien, P. K. Light Waves in Thin Films and Integrated Optics. Applied Optics, 1971. Vol. 10, pp. 2395–2413.

[89] Ulrich, R. and Torge, R. Measurement of Thin Film Parameters with a Prism Coupler. Applied Optics, 1973. Vol. 12, pp. 2901–2908.

[90] Adachi, H., Kawaguchi, T., Setsune, K., Ohji, K. and Wasa, K. Electro-optic effects of $(Pb,La)(Zr,Ti)O_3$ thin films prepared by RF palanar magnetron sputtering. Applied Physics Letters, 1983. Vol. 42, pp. 867–868.

[91] Haertling, G. H. PLZT Electrooptic Materials and Applications – a Review. Ferroelectrics, 1987. Vol. 75, pp. 25–55.

[92] Yi, G., Wu, Z. and Sayer, M. Preparation of $Pb(Zr,Ti)O_3$ thin films by sol gel processing: Electrical, optical, and electro-optic properties. Journal of Applied Physics, 1988. Vol. 64, pp. 2717–2724.

[93] Kololuoma, T., Hiltunen, J., Tuomikoski, M., Lappalainen, J. and Rantala, J. Directly UV-photopatternable PLZT thin films prepared with the Sol-Gel technique. Proceedings of SPIE. Vol. 5355. Integrated Optics: Devices, Materials, and Technologies VIII, 2004, pp. 33–39.

[94] Moret, M. P., Devillers, M. A. C., Wörhoff, K. and Larsen, P. K. Optical properties of $PbTiO_3$, $PbZr_xTi_{1-x}O_3$ and $PbZrO_3$ films deposited by metalorganic chemical vapour on $SrTiO_3$. Journal of Applied Physics, 2002. Vol. 92, pp. 468–474.

[95] Chattopadhyay, S., Aytub, P., Palkar, V. R. and Multani, M. Size-induced diffuse phase transition in the nanocrystalline ferroelectric $PbTiO_3$. Physical Review B, 1995. Vol. 52, pp. 13177–13183.

[96] Lappalainen, J., Lantto, V., Frantti, J. and Hiltunen, J. X-ray diffraction and Raman investigations of thickness dependent stress effects on $Pb(Zr_xTi_{1-x})O_3$ thin films. Applied Physics Letters, 2006. Vol. 88, Article 252901.

[97] Tang, P., Towner, D. J., Meier, A. L. and Wessels, B. W. P. $BaTiO_3$ thin-film waveguide modulator with a low voltage-length product at near-infrared wavelengths of 0.98 and 1.55 μm. Optics Letters, 2005. Vol. 30, pp. 254–256.

[98] Harigai, T., Tanaka, D., Kakemoto, H., Wada, S. and Tsurumi, T. Dielectric properties of $BaTiO_3/SrTiO_3$ superlattices measured with interdigital electrodes and electromagnetic field analysis. Journal of Applied Physics, 2003. Vol. 94, pp. 7923–7925.

[99] Tsurumi, T., Ichikawa, T., Harigai, T., Kakemoto, H. and Wada, S. Dielectric and optical properties of $BaTiO_3/SrTiO_3$ and $BaTiO_3/BaZrO_3$ superlattices. Journal of Applied Physics, 2002. Vol. 91, pp. 2284–2289.

[100] Sarkar, A. and Krupanidhi, S. B. Ferroelectric interaction and polarization studies in $BaTiO_3/SrTiO_3$ superlattice. Journal of Applied Physics, 2007. Vol. 101, Article 104113.

[101] Kim, B. R., Kim, T.-U., Lee, W.-J., Moon, J. H., Lee, B.-T., Kim, H. S. and Kim, J. H. Effects of periodicity and oxygen partial pressure on the crystallinity and dielectric property of artificial $SrTiO_3/BaTiO_3$ superlattices integrated on Si substrates by pulsed laser deposition. Thin Solid Films, 2007. Vol. 515, pp. 6438–6441.

[102] Tyunina, M., Jaakola, I., Levoska, J. and Plekh, M. Diffuse phase transitions in epitaxial $(Ba,Sr)TiO_3$ superlattices. Physical Review B, 2007. Vol. 76, Article 134107.

[103] Haeni, J. H., Irvin, P., Uecker, R., Reiche, P., Li, Y. L., Choudhury, S., Tian, W., Hawley, M. E., Craigo, B., Tagantsev, A. K., Pan, A. Q., Streiffer, S. K., Chen, L. Q., Kirchoefer, S. W., Levy, J. and Schlom, D. G. Room-temperature ferroelectricity in strained $SrTiO_3$. Nature, 2004. Vol. 430, pp. 758–760.

[104] Johnston, K., Huang, X., Neaton, J. B. and Rabe, K. M. First-principles study of symmetry lowering and polarization in $BaTiO_3/SrTiO_3$ superlattices with in-plane expansion. Physical Review B, 2005. Vol. 71, Article 100103.

[105] Lisenkov, S. and Bellaiche, L. Phase diagrams of $BaTiO_3/SrTiO_3$ superlattices from first principles. Physical Review B, 2007. Vol. 76, Article 020102.

[106] Kim, L., Kim, J., Waghmare, U. V., Jung, D. and Lee, J. Structural transition and dielectric response of an epitaxially strained $BaTiO_3/SrTiO_3$ superlattice: A first principles study. Physical Review B, 2005. Vol. 72, Article 214121.

[107] Vaithyanathan, V., Lettieri, J., Sharan, A., Vasudevarao, A., Li, Y. L., Kochhar, A., Ma, H., Levy, J., Zschack, P., Woicik, J. C., Chen, L. Q., Gopalan, V. and Schlom, D. G. *c*-axis oriented epitaxial $BaTiO_3$ films on (001) Si. Journal of Applied Physics, 2006. Vol. 100, Article 024108.

[108] Gaidi, M., Stafford, L., Margot, J., Chker, M., Morandotti, R. and Kulishov, M. Microfabricated $SrTiO_3$ ridge waveguides. Applied Physics Letters, 2005. Vol. 86, Article 221106.

Appendices I–V of the publication are not included in this PDF version. Please order the printed version to get the complete publication (http://www.vtt.fi/publications/index.jsp)

Series title, number and report code of publication

VTT Publications 684
VTT-PUBS-684

Author(s)
Hiltunen, Jussi

Title

Microstructure and superlattice effects on the optical properties of ferroelectric thin films

Abstract

This thesis deals with the microstructure effects on the optical properties of (i) polycrystalline Nd-modified lead-zirkonium-titanate (PNZT) and (ii) highly oriented $BaTiO_3$ (BTO) thin films together with the stacking structure influence on the optical properties of (iii) $BaTiO_3$–$SrTiO_3$ (STO) superlattice thin films. All the films were grown on MgO(001) substrates by pulsed laser deposition. Different structures were obtained by tuning the thin film processing conditions.

PNZT thin films were deposited at room temperature and different crystallite size distributions were produced by varying the post-annealing temperature. The refractive index and electro-optic responses were found to increase with increasing mean crystallite size.

Oxygen pressure during the film deposition at 700 °C was found to be a very critical parameter to modify the crystallographic and consequent other physical properties of BTO thin films as suggested by the dielectric and optical measurements. Low oxygen pressure films were epitaxial, with elongated lattice parameters along the surface normal, while increased working oxygen pressure produced non-epitaxial films with lattice elongation along the in-plane orientation. An effective electro-optic coefficient of ~21 pm/V was measured for the BTO films.

Periodic BTO-STO superlattices were deposited with varying stacking periodicity between 27 and 1670 Å. Birefringence decreased with increasing stacking periodicity, due to relaxation of the lattice strain induced by the layer interfaces. The electro-optic response was found to reach a maximum at a specific stacking periodicity and it decreases with both increasing and decreasing individual layer thickness. The operation of a Mach-Zehnder waveguide intensity modulator based on the BTO-STO superlattice with effective electro-optic coefficient of 73 pm/V was also demonstrated.

ISBN
978-951-38-7102-4 (soft back ed.)
978-951-38-7103-1 (URL: http://www.vtt.fi/publications/index.jsp)

Series title and ISSN	Project number
VTT Publications 1235-0621 (soft back ed.) 1455-0849 (URL: http://www.vtt.fi/publications/index.jsp)	25779

Date	Language	Pages
June 2008	English	82 p. + app. 42 p.

Name of project	Commissioned by
Optoferro	Tekes, Infotech Oulu, the Academy of Finland, Finnish Foundation for Technology Promotion, Tauno Tönningin säätiö, Emil Aaltosen säätiö, Seppo Säynäjäkankaan tiedesäätiö

Keywords	Publisher
ferroelectrics, thin film, electro-optics, superlattice, PZT, $BaTiO_3$, $SrTiO_3$	VTT Technical Research Centre of Finland P.O.Box 1000, FI-02044 VTT, Finland Phone internat. +358 20 722 4520 Fax +358 20 722 4374

This thesis deals with the microstructure effects on the optical properties of *(i)* polycrystalline Nd-modified lead-zirkonium-titanate (PNZT) and *(ii)* highly oriented $BaTiO_3$ (BTO) thin films together with the stacking structure influence on the optical properties of *(iii)* $BaTiO_3$–$SrTiO_3$ (STO) superlattice thin films. All the films were grown on MgO(001) substrates by pulsed laser deposition. Different structures were obtained by tuning the thin film processing conditions.

PNZT thin films were deposited at room temperature and different crystallite size distributions were produced by varying the post-annealing temperature. The refractive index and electro-optic responses were found to increase with increasing mean crystallite size.

Oxygen pressure during the film deposition at 700 °C was found to be a very critical parameter to modify the crystallographic and consequent other physical properties of BTO thin films as suggested by the dielectric and optical measurements. Low oxygen pressure films were epitaxial, with elongated lattice parameters along the surface normal, while increased working oxygen pressure produced non-epitaxial films with lattice elongation along the in-plane orientation. An effective electro-optic coefficient of ~21 pm/V was measured for the BTO films.

Periodic BTO-STO superlattices were deposited with varying stacking periodicity between 27 and 1670 Å. Birefringence decreased with increasing stacking periodicity, due to relaxation of the lattice strain induced by the layer interfaces. The electro-optic response was found to reach a maximum at a specific stacking periodicity and it decreases with both increasing and decreasing individual layer thickness. The operation of a Mach-Zehnder waveguide intensity modulator based on the BTO-STO superlattice with effective electro-optic coefficient of 73 pm/V was also demonstrated.

Julkaisu on saatavana
VTT
PL 1000
02044 VTT
Puh. 020 722 4520
http://www.vtt.fi

Publikationen distribueras av
VTT
PB 1000
02044 VTT
Tel. 020 722 4520
http://www.vtt.fi

This publication is available from
VTT
P.O. Box 1000
FI-02044 VTT, Finland
Phone internat. + 358 20 722 4520
http://www.vtt.fi

ISBN 978-951-38-7102-4 (soft back ed.)
ISSN 1235-0621 (soft back ed.)

ISBN 978-951-38-7103-1 (URL: http://www.vtt.fi/publications/index.jsp)
ISSN 1455-0849 (URL: http://www.vtt.fi/publications/index.jsp)